IMMUNOLOGY

A beneficial environment promotes immune resilience through epigenetic regulation

Guilherme Dragunas[1,2]†, Markus Klotz[1,2]†, Sirui Chen[1,2]†, Zeynep Ertüz[1,2], Xiaomei Tan[1,2], Ülkü Rabia Korkmaz[3], Soni Shankhwar[3], Bettina Rankl[3], Deepesh Dhakad[1,2], Jimmy Omony[3], Christoph H. Mayr[1,2,4], Yuexin Chen[1,2,4], Ahmed Agami[1,2,4], Chung-Wen Lin[5], Christoph Müller[6], Lars Lunding[7,8], Michael Wegmann[2,7], Johanna Berner[9,10], Jelena Popovic[9,10], Barbara U. Schraml[9,10], Heiko Adler[2,3,11], Pascal Falter-Braun[5,12], Herbert Schiller[1,2,4,13], Henrik Watz[14,15], Thomas M. Conlon[1,2], Aicha Jeridi[1,2], Theodoros S. Kapellos[1,2,13], Erika von Mutius[2,3,16]‡, Ali Önder Yildirim[1,2,13]*‡

Environmental factors are often detrimental; however, certain environments enhance immune resilience. Notably, children raised on traditional farms show reduced allergies and asthma prevalence. Here, we investigated how a beneficial environment, using farm dust (FD) extract, influenced lung immune function in ovalbumin-induced allergic inflammation. FD exposure reduced allergic lung inflammation and increased monocyte-derived macrophage (MDM) recruitment. Single-cell RNA sequencing revealed that FD-exposed MDMs had altered gene expression, including dampened *Ccl8* and major histocompatibility complex class II expression, impairing eosinophil recruitment and antigen presentation. RNA sequencing and assay for transposase-accessible chromatin using sequencing confirmed FD-induced epigenetic reprogramming ex vivo, on bone marrow–derived macrophages. This modulation, seen in both human and murine cells, relied on histone deacetylase activity sustained by peroxisome proliferator–activated receptor γ signaling. These findings suggest that beneficial environmental exposures can reprogram immune cells and may offer a previously unidentified strategy for asthma prevention.

INTRODUCTION

Environmental exposure is a key determinant of long-term immune modulation that skews immune cells toward activation or tolerance and is ultimately influencing disease susceptibility and health. Asthma and allergic disorders still represent a pressing public health concern (*1*, *2*), and their incidence is strongly associated with environmental cues, either deleterious, such as pollution or viral infections, or beneficial, as observed in children raised in traditional farm environments (*3*). Dysregulation of antigen-presenting cells (APCs) through major histocompatibility complex class II (MHCII) represents a hallmark of allergic asthma (*4*). This leads to the activation of $CD4^+$ T helper 2 (T_H2) cells, the subsequent recruitment of eosinophils, and the development of airway hyperresponsiveness (AHR) (*5*). Children raised in the farm environment, particularly those in close contact with livestock, showed a significant reduced asthma risk; this has been attributed to exposure to airborne and surface-deposited farm dust (FD) and its components (*6*, *7*). Here, we decipher the underlying mechanism by which sustained environmental exposure to FD extract induces protection against allergic asthma. We demonstrate that FD exposure recruits APCs and induces epigenetic silencing of both antigen presentation and eosinophil chemoattractant *Ccl8* expression through a peroxisome proliferator–activated receptor (PPAR)–regulated, histone deacetylase (HDAC)–dependent axis. These insights provide a mechanistic basis for the beneficial protective effects of farm environments and open different avenues for intervention strategies targeting asthma prevention.

RESULTS

Protective exposure to FD extract regulates monocyte-derived macrophages

As a model for the beneficial farm environment in protecting against allergic asthma, we preventively administered FD extract, isolated from traditional farms and autoclaved, to mice in the ovalbumin (OVA)–induced allergic asthma model (fig. S1A). Mice that received intranasal applications of FD extract (OVA + FD) revealed reduced AHR (Fig. 1A), accompanied by reduced numbers of eosinophils both in bronchoalveolar lavage (BAL) (Fig. 1, B and C) and lung tissue sections (fig. S1B). In addition, periodic acid–Schiff–positive (PAS^+) mucus-producing goblet cells (Fig. 1, B and D) and mucus-associated genes (*Muc5ac* and *Gob5*) (fig. S1C) were significantly reduced

[1]Institute of Lung Health and Immunity (LHI), Helmholtz Munich, Comprehensive Pneumology Center (CPC-M), Munich, Germany. [2]Member of the German Center of Lung Research (DZL), Munich, Germany. [3]Institute for Asthma and Allergy Prevention, Helmholtz Center Munich, German Research Center for Environmental Health, Munich, Germany. [4]Research Unit Precision Regenerative Medicine (PRM), Helmholtz Munich, Munich, Germany. [5]Institute of Network Biology (INET), Molecular Targets and Therapeutics Center (MTTC), Helmholtz Center Munich, German Research Center for Environmental Health, Munich, Germany. [6]Department of Pharmacy, Center for Drug Research, Ludwig-Maximilian's University, LMU, Munich, Germany. [7]Division of Lung Immunology, Priority Area Chronic Lung Diseases, Research Centre Borstel–Leibniz Lung Centre, Borstel, Germany. [8]Airway Research Center North, Member of the German Centre for Lung Research (DZL), Germany. [9]Institute for Immunology, Biomedical Center Munich, Faculty of Medicine, LMU Munich, Munich, Planegg-Martinsried, Germany. [10]Biomedical Center, Institute of Cardiovascular Physiology and Pathophysiology, Faculty of Medicine, LMU Munich, Munich, Germany. [11]Walther Straub Institute of Pharmacology and Toxicology, Ludwig-Maximilians-University Munich, Member of the German Center of Lung Research (DZL), Munich, Germany. [12]Microbe-Host Interactions, Faculty of Biology, Ludwig-Maximilians-Universität (LMU) München, Munich, Germany. [13]Institute of Experimental Pneumology, LMU University Hospital, Ludwig-Maximilian's University, Munich, Germany. [14]Velocity Clinical Research Germany, Ahrensburg, Germany. [15]University of Lübeck, Airway Research Center North (ARCN), German Center for Lung Research (DZL), Lübeck, Germany. [16]Department of Pediatrics, Dr. von Hauner Children's Hospital, LMU University Hospital, LMU Munich, Munich, Germany.
*Corresponding author. Email: oender.yildirim@helmholtz-munich.de
†These authors contributed equally to this work.
‡These authors contributed equally to this work.

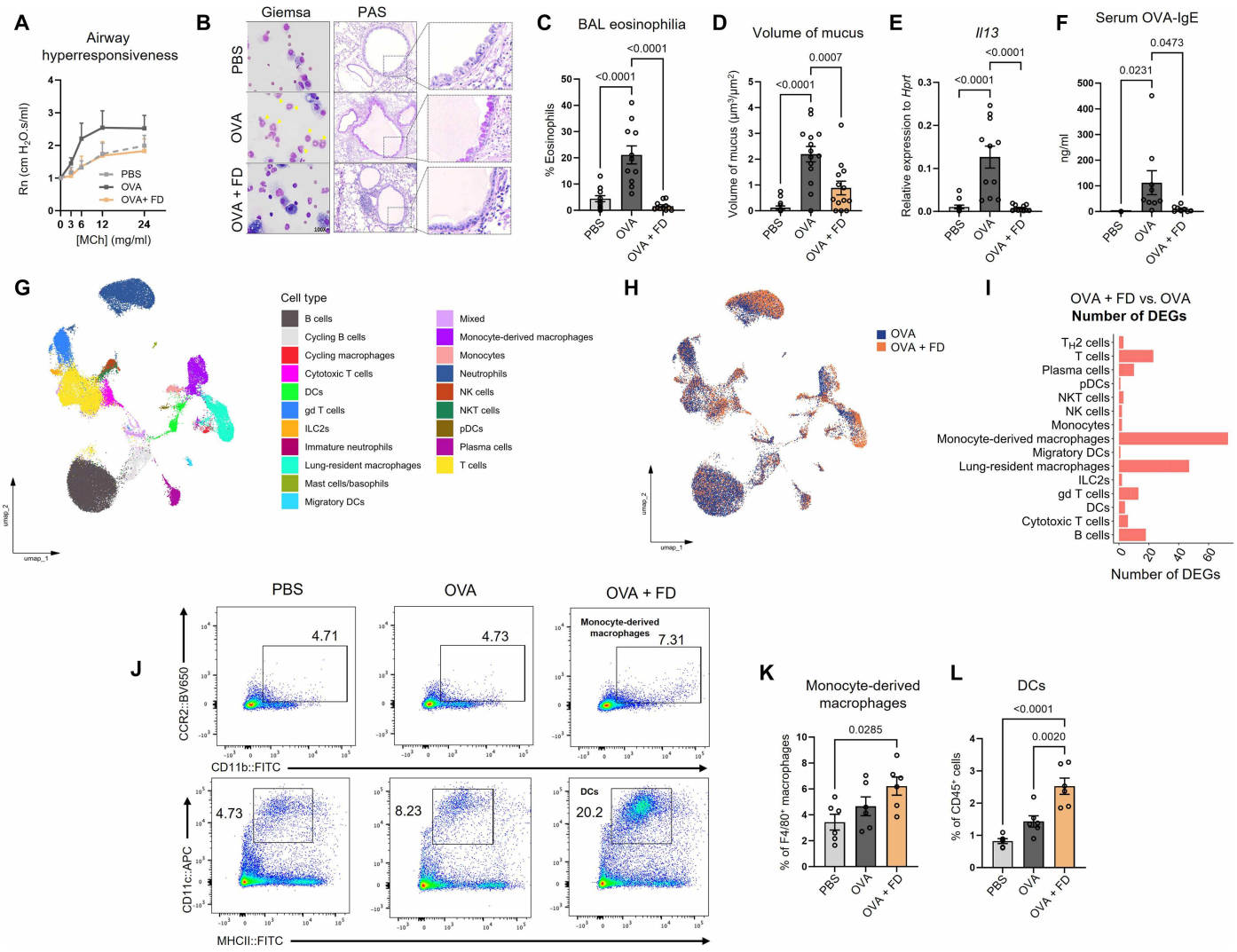

Fig. 1. Preventive exposure to FD reduces allergic sensitization to OVA and induces the recruitment of transcriptionally altered macrophages and DCs to the lungs. (**A**) Airway resistance measured after increasing concentrations of nebulized methacholine to anesthetized mice. (**B**) Representative BAL differential counts and PAS staining images and (**C**) quantification of BAL eosinophilia and (**D**) volume of mucus within airway epithelium. (**E**) Reverse transcription quantitative polymerase chain reaction (RT-qPCR) analysis from whole-lung homogenates detecting the expression of *Il13* gene. (**F**) Serum titers of anti-OVA–specific IgE. (**G**) Annotated immune cells were subsetted from whole-lung scRNA-seq and 2D plotted using uniform manifold approximation and projection for dimension reduction (UMAP). (**H**) OVA and OVA + FD immune cell UMAP representation overlaid. (**I**) DEG number comparing OVA versus OVA + FD groups. (**J**) Representative flow cytometry plots highlighting MDM and DC identification and (**K** and **L**) quantification of frequency of these cell types within parent gates. Results are plotted as means ± SEM, and difference between means were compared using one-way analysis of variance (ANOVA) followed by Tukey's post hoc test ($n = 6$ to 9).

following pretreatment with FD extract. Consistent with this, the expression of asthma-related cytokines *Il13* (Fig. 1E), *Il4*, *Il5*, and *Il33* (fig. S1D) was also decreased. Furthermore, reduced serum anti-OVA–specific immunoglobulin E (IgE) (Fig. 1F) and IgG1 (fig. S1E) were also observed, indicating FD-mediated prevention of allergic sensitization. To elucidate the mechanism of beneficial FD extract on asthma prevention, we sequenced 61,803 cells isolated from the lungs of the allergic asthma model (fig. S1F). Immune cells were annotated for downstream analysis (fig. S1G), followed by clustering using uniform manifold approximation and projection (UMAP) (Fig. 1G). The distribution of immune cells, particularly the frequency of macrophages and dendritic cells (DCs), increased following FD exposure (Fig. 1H). Notably, the most significant regulation in differentially expressed genes (DEGs) was observed specifically in monocyte-derived macrophages (MDMs) and lung-resident macrophages (LRMs) (Fig. 1I). This was confirmed by an increased presence of $CD68^+$, $CD11b^+$, and $CD11c^+$ cells around airways in lung tissue sections of FD-exposed mice, indicating heightened presence of recruited macrophages and DCs (fig. S1, H and I). Last, we validated these findings in flow cytometry of lung tissue, observing an increased presence of $CD45^+$, $Ly6g^{neg}$, $Ly6c^+$, $CD11c^{neg}$, $SiglecF^{neg}$, $CD11b^+$, $CCR2^+$, and MDMs and $CD45^+$, $CD11c^+$, and $MHCII^+$ DCs in FD-exposed lungs (Fig. 1, J to L). Conversely (fig. S1J), the number of alveolar LRMs (fig. S1K), $CD103^+$ conventional type 1 DCs (cDC1s), and $CD11b^+$ cDC2s (fig. S1L) were not significantly altered. Collectively, these data suggested that FD exposure induced

allergic asthma prevention through a distinct regulation of MDMs, suggesting a potential role in modulating the allergic response.

FD exposure regulates *Ccl8* in MDMs

To determine the role of MDMs in allergic asthma prevention, we used *Ccr2*$^{-/-}$ mice, which demonstrated reduced MDM recruitment to the lung following OVA sensitization (fig. S2A). This was accompanied by protection from OVA-induced AHR (fig. S2B), BAL eosinophilia (fig. S2C), mucus hyperplasia (fig. S2D), and mucus-associated gene expression compared with wild-type (WT) control mice treated with OVA (fig. S2E), thus suggesting that MDMs play a causative role in allergy prevention. Therefore, we assessed the DEG pattern in MDMs from the single-cell RNA sequencing (scRNA-seq) data. The most down-regulated gene in MDMs from FD-exposed mice compared to OVA controls was the chemokine *Ccl8* followed by *Retnla* and MHCII-related molecules—*Ciita*, *H2-Aa*, *H2-Ab1*, and *H2-Eb1* (Fig. 2A). Furthermore, we observed that the expression of *Ccl8* was predominantly restricted to MDMs (fig. S2F). The CCL8-CCR8 axis was previously reported to induce tissue recruitment of eosinophils and T_H2 cells in eosinophilic skin inflammation (*8*). scRNA-seq shows that FD exposure significantly reduced the expression levels of the *Ccl8* gene in MDMs (Fig. 2B). Consistently, *Ccl8* gene expression in whole mouse lungs (fig. S2G) and CCL8 protein levels in serum of OVA + FD mice were significantly reduced,

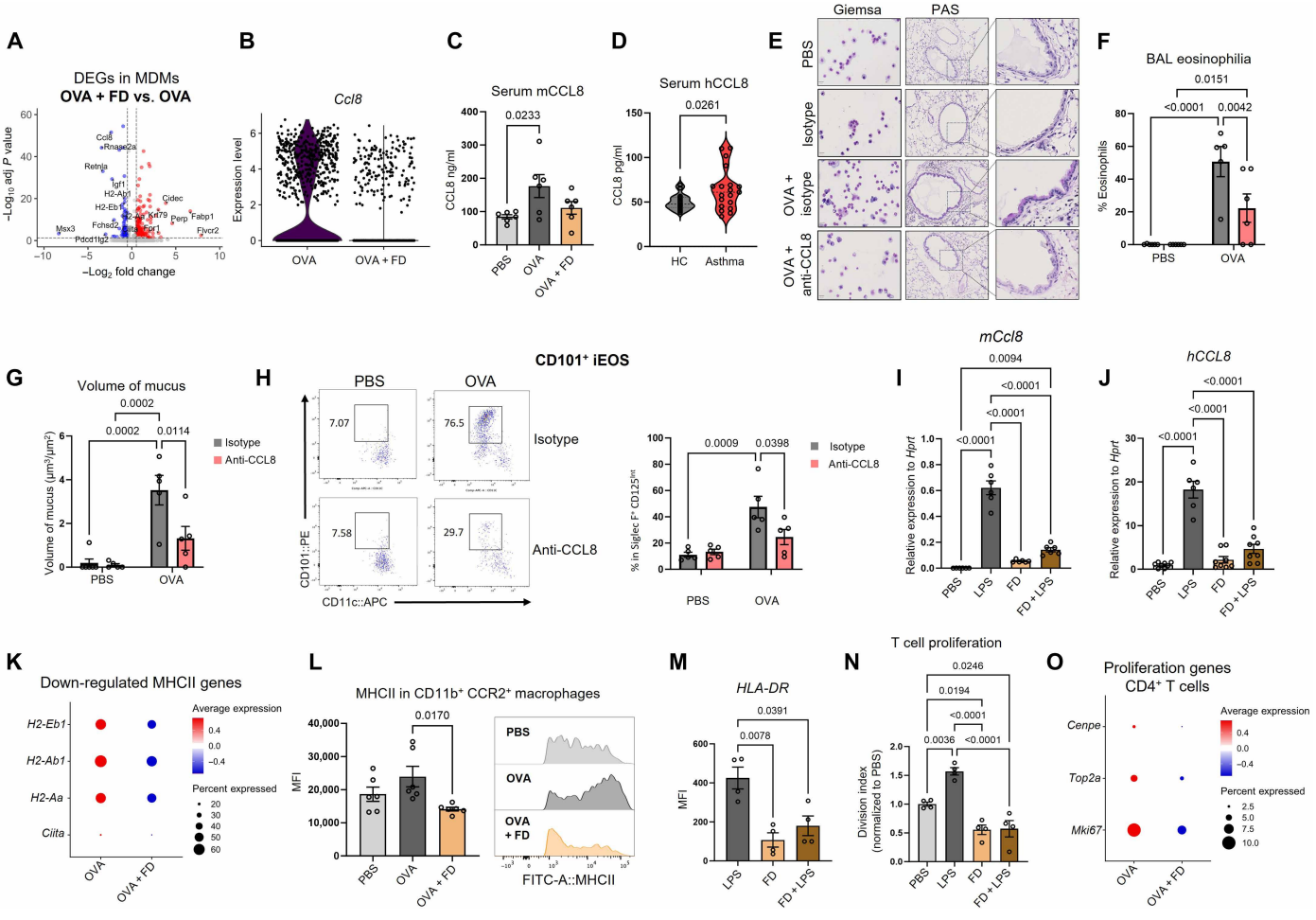

Fig. 2. Preventive exposure to FD leads to changes in MDM transcriptome that are associated with reduced CCL8 production and MHCII-mediated antigen presentation. (**A**) Volcano plot showing DEGs in OVA versus OVA + FD MDMs, analyzed by model-based analysis of single-cell transcriptomics (MAST). (**B**) *Ccl8* gene expression in OVA versus OVA + FD. (**C**) Mouse serum CCL8 measured by enzyme-linked immunosorbent assay. (**D**) Serum CCL8 levels in human patients with asthma versus healthy controls. (**E**) WT mice were sensitized to OVA and treated daily with anti-CCL8 antibody or isotype 6 hours before OVA challenge. Representative BAL Giemsa cytospins and PAS-stained lung sections are shown. (**F**) Quantification of BAL eosinophils and (**G**) volume of mucus. (**H**) Lung inflammatory eosinophils (CD45$^+$, Ly6g^{neg}, CD125^{int}, SiglecF$^{+,}$ CD11c$^+$, and CD101$^+$) quantified by flow cytometry. (**I** and **J**) CCL8 gene expression in murine BMDMs and human monocytes after 48 hours of FD exposure followed by 6 hours of LPS stimulation. (**K**) Average gene expression from MHCII-related genes (*H2-Eb1*, *H2-Ab1*, *H2-Aa*, and *Ciita*) were down-regulated in OVA + FD MDMs. (**L**) MHCII mean fluorescence intensity (MFI) on lung MDMs (CD45$^+$, F4/80$^+$, Ly6G^{neg}, CD11b$^+$, and CCR2$^+$). (**M**) HLA-DR MFI in human monocyte–derived APCs exposed to FD for 48 hours and LPS for 6 hours. (**N**) BMDMs pulsed with $OVA_{323–339}$ peptide after FD and LPS stimulation and then cocultured with naive CD4$^+$ T cells. T cell proliferation assessed by CellTrace™ Violet (CTV) MFI-based division index. (**O**) Proliferation-associated gene (*Cenpe*, *Top2a*, and *Mki67*) average expression within CD4$^+$ T cell subset in OVA versus OVA + FD. Modules were clustered by KEGG/Reactome terms; antigen presentation node shows altered interaction strength. Results are plotted as means ± SEM, and difference between means were compared using one-way ANOVA followed by Tukey's post hoc test (n = 4 to 19).

compared with OVA mice (compared with OVA; Fig. 2C). We also measured CCL8 protein levels in serum of patients with asthma and observed these to be significantly elevated in comparison with healthy control human serum samples (Fig. 2D). Gene counts from other chemokines reported to attract T_H2 cells and eosinophils, namely, *Ccl24*, *Ccl5*, and *Ccl11* within MDMs were also assessed; however, their expression was barely detectable (fig. S2H), indicating the relevance of CCL8.

To investigate the significance of CCL8 in allergic asthma development, we treated daily OVA-sensitized mice with intraperitoneal injections of 5 μg of CCL8-blocking antibody (anti-CCL8) or isotype control (rat IgG2k) (fig. S2I). CCL8 blockade reduced BAL eosinophilia and airway goblet cell hyperplasia (Fig. 2, E to G) and AHR (fig. S2J). Crucially, fluorescence-activated cell sorting (FACS) analysis revealed that CCL8 blockade significantly reduced the migration of $CD101^+$ inflammatory eosinophils to the lungs (Fig. 2H and fig. S3A), whereas $CD101^{neg}$-resident eosinophils or $CD4^+$ effector T cell numbers remained unchanged (figs. S2K and S3B). Collectively, these data suggest that CCL8 secretion from MDMs attract inflammatory eosinophils, inducing mucus production and AHR. To investigate the regulators of *Ccl8*, we used CistromeDb (*9*) to identify the potential transcription factors (TFs) that bind the promoter region of *Ccl8*. We identified potential transcriptional regulation of *Ccl8* by nuclear factor κB and signal transducers and activators of transcription, as indicated by their binding to the *Ccl8* promoter (fig. S2L). To investigate this, we stimulated murine bone marrow–derived macrophages (BMDMs) with lipopolysaccharide (LPS), which strongly up-regulated *Ccl8* expression in a Toll-like receptor 4 (TLR4)–dependent manner. This up-regulation was completely abrogated by pretreatment with the TLR4 inhibitor resatorvid (1 μM) (fig. S2M). Further, the inhibition of TLR2 in BMDMs did not reverse the effect of FD + LPS–induced effect on Ccl8 expression, confirming that TLR4, rather than TLR2, is the predominant upstream receptor regulating *Ccl8* expression in our system (fig. S2N). Crucially, LPS-induced expression of *Ccl8* in murine BMDM was abolished once FD pretreatment was added (Fig. 2I). Translationally, we also used human peripheral blood mononuclear cell (PBMC)–derived monocytes exposed to LPS, where pretreatment with FD extract similarly abrogated both *CCL8* gene (Fig. 2J) and secreted protein levels (fig. S2O), indicating a common mechanism in both murine and human cells.

Down-regulation of MHCII genes in response to FD

MHCII-restricted antigen presentation is crucial for allergic sensitization and accompanying the reduced *Ccl8* expression. We observed strong down-regulation of MHCII family–related genes *Ciita*, *H2-Aa*, *H2-Ab1*, and *H2-Eb1* (Fig. 2K) in FD-exposed MDMs from the scRNA-seq analysis. Supporting this, Kyoto Encyclopedia of Genes and Genomes (KEGG) pathway enrichment of the scRNA-seq data demonstrated a suppression of the Asthma (mmu05310) and Antigen Processing and Presentation (mmu04612) pathways in FD-exposed MDMs compared with OVA alone (fig. S4A). A combined score for all MHCII-associated gene expression in MDMs additionally supports a reduction in MHCII following exposure to FD extract (fig. S4B). Flow cytometry analysis of whole-lung homogenates demonstrated a significant reduction of MHCII surface expression on $CD11b^+$ $CCR2^+$ MDMs from FD-exposed mice (Fig. 2L). Crucially, human PBMC-derived monocytes pretreated with FD extract prevented *HLA-DR* membrane expression (Fig. 2M). To confirm a functional role, we cocultured MHCII-restricted $OVA_{323–339}$-pulsed BMDMs with naïve splenic T $CD4^+$ cells from OT-II mice and observed that pretreatment with FD abrogated the proliferation of OT-II cells (Fig. 2N).

To investigate further, we subclustered T cells in our scRNA-seq data to annotate CM (central memory) $CD4^+$, CM $CD8^+$, T follicular helper cells, T_H2 cells, $Foxp3^+$ regulatory T cells, and $Cxcr6^+$ $Ctla4^+CD4^+$ T cells (fig. S4, C to E). We observed a significant suppression of KEGG terms related to T cell proliferation, activation, and T_H2 differentiation in the $CD4^+$ T cells from FD-exposed mice (fig. S4F). The reduction of OT-II proliferation was mirrored by the reduction of T cell proliferation (Fig. 2O and fig. S4G) and activation-related genes (fig. S4, H and I) in $CD4^+$ T cells from scRNA-seq data of the FD-exposed mice. Whole-lung homogenates from OVA + FD mice showed a reduction in the number of $CD3^+$ and $CD4^+$ T cells compared with OVA alone (fig. S4, J and K), while immunostaining against CD4 and Ki67 confirmed reduced numbers of proliferating $CD4^+$ T cells in the lung of FD-exposed mice (fig. S4, L and M).

Thus far, we have revealed the importance of MDMs in regulating the allergic response. Classically, DCs are the APCs contributing to T cell activation in allergic asthma. We therefore subclustered DCs from scRNA-seq data of the allergic asthma mouse model with FD exposure, identifying migratory DCs, cDC1, cycling cDC1, cDC2, and plasmacytoid dendritic cells (pDCs) cell populations (fig. S5, A to C). Despite no difference in frequencies, we observed suppression of the KEGG term Asthma and T_H1 and T_H2 cell differentiation in migratory DCs from FD-exposed mice (fig. S5D), which was accompanied by a reduction in the expression of MHCII genes *H2-Aa* and *H2-Eb1* (fig. S5E). MHCII expression was further evaluated by flow cytometry and found to be down-regulated in monocyte-derived DCs and $Cd11b^+$ cDC2 cells (fig. S5F). For functional analysis, we differentiated mouse bone marrow–derived DCs (BMDCs) and cocultured with naïve splenic $CD4^+$ T cells from OT-II mice after pulsing with $OVA_{323–339.}$ Similar to BMDMs, the BMDCs also displayed dampened capacity to expand OT-II $CD4^+$ T cells (fig. S5G) and down-regulated MHCII surface expression in response to FD (fig. S5H).

Next, to evaluate that FD-exposed BMDMs are crucial for allergen sensitization, we intratracheally transferred FD-treated BMDMs or BMDCs pulsed with OVA to naïve mice and challenged them intranasally with OVA 7 days later. FD-exposed BMDMs significantly lowered total BAL eosinophilia (fig. S6, A and B), compared with OVA-pulsed BMDMs not pretreated with FD. However, FD-pulsed BMDCs did not show any preventive effects upon the OVA-induced allergic asthma model (fig. S6, C and D). To confirm that BMDMs were crucial to FD-dampened allergic sensitization, we intratracheally transferred a mix of BMDMs and BMDCs pretreated with or without FD and OVA pulsed, into mice that were subsequently challenged intranasally with OVA (fig. S6E). We clearly observed that combined BMDM and BMDC administration, where both or only BMDMs were treated with FD, prevented OVA-induced total BAL count recovery (fig. S6F) and BAL eosinophilia (fig. S6, G and H) and down-regulated the type 2–associated cytokine genes *Il4* and *Il13* (fig. S6I). A similar effect was also observed for *Ccl8* expression (fig. S6J), the mucus-associated genes *Muc5ac* and *Spdef* (fig. S6K), and macrophage MHCII surface expression (fig. S6L). We additionally detected reduced expression of M2-related membrane protein CD206 in the same groups within lung macrophages (fig. S6M).

Considering the DC lung population, these groups were associated with reduced surface expression of MHCII (fig. S6N) and dampened frequency of both $CD103^+$ cDC1 and $CD11b^+$ cDC2 populations (fig. S6O). While transfer of both cell types simultaneously mediated FD protection, protection was also provided only upon FD exposure of the BMDMs. FD treatment of BMDMs did not affect their cell viability (fig. S6P). Together, FD exposure regulates MHCII complex and *Ccl8* gene expression in MDMs and impairs their ability to regulate eosinophil recruitment, AHR, and T cell activation and proliferation in allergic asthma, with BMDCs playing a minor role.

Epigenetic remodeling in BMDMs confers FD-mediated transcriptome

To further elucidate the molecular mechanisms underlying FD-exposed MDMs in modulating the allergic response, we performed bulk RNA sequencing (RNA-seq) and assay for transposase-accessible chromatin using sequencing (ATAC-seq) on BMDMs and BMDCs, which we treated with FD extract and activated with LPS (fig. S7A). BMDMs showed a unique transcriptomic profile after FD treatment, as highlighted in unbiased clustering of highly variable genes (fig. S7B) and two-dimensional (2D) principal components analysis (PCA) plot analysis (fig. S7C). Comparison between conditions using DESeq2 showed a robust modulation of gene expression (fig. S7D) and confirmed that antigen processing and presentation and MHCII-related genes were down-regulated in FD-exposed BMDMs (fig. S7, E and F). Similarly, genes from the Asthma KEGG pathway (mmu-05310) and proinflammatory genes, including *Ccl8*, were down-regulated in FD-pretreated BMDMs (fig. S7, G and H). Furthermore, to validate these findings, we integrated protein-protein interactome networks from KEGG pathways to analyze protein modules that interacted with higher or lower strength. Here, when FD was added to the system, the connected nodes from MHCII proteins displayed decreased interaction strength (Fig. 3A), validating that MHCII down-regulation is a specific and prominent effect of FD exposure in BMDMs. PCA clearly revealed spatial separation between samples and a significant gene expression difference in the FD-treated BMDCs (fig. S8A). The FD effect on BMDCs in vivo was equally pronounced (fig. S8, B and C). Similarly, we also observed lowered gene expression from MHCII genes after exposure of BMDCs to FD, which are crucial for allergy development and T_H2 differentiation (fig. S8, D and E). Furthermore, the protein-protein interactome analysis provided a similar pattern with reduced MHCII protein interactions (fig. S8F).

We clearly observed that repetitive exposure to FD extract led to a stronger response (fig. S9, A and B). Therefore, we sought to understand whether epigenetic regulation was mediating the FD-induced prevention of allergy. To test this, we undertook ATAC-seq upon the BMDMs, which revealed no global effect of FD on chromatin accessibility (fig. S9C), nor a differential peak distribution within gene features (fig. S9D). To gain further insight into differential regulation of accessibility, we performed normalization and pairwise comparison of differential open chromatin regions (OCRs) using DESeq2. This revealed that the changes in OCRs were reduced upon FD extract pretreatment (Fig. 3, B and C) and clustered separately from LPS-activated BMDMs in a 2D PCA plot (fig. S9E). Further, closed chromatin was observed for multiple genes after FD exposure (Fig. 3D). Next, peaks with lower accessibility (loss) were annotated, and motif enrichment analysis was performed using HOMER (*10*). This revealed that motifs associated to interferon regulatory factor 1 (IRF1), IRF2, IRF3, IRF8, PU.1, and the PU.1: IRF8 heterodimer were significantly more present within regions that are closed in FD-exposed cells (Fig. 3, E and F). IRFs are, especially IRF4 and IRF8, potent inducers of MHCII gene expression and are known to bind pIII and pIV promoters from *Ciita* in myeloid APCs to stimulate the expression of MHCII genes (*11*–*13*). *Ciita* regulation involves epigenetic mechanisms to counterbalance PU.1: IRF8 binding (*12*), and HDAC1 and HDAC2 have also been shown to crucially regulate the expression of MHCII genes via deacetylation of *Ciita* (*14*).

Next, we merged the data from RNA-seq and ATAC-seq assays, using common annotated gene names as anchor points. We observed a significant linear relationship between ATAC-seq OCRs and RNA-seq data, which demonstrated a significant down-regulation and closing of MHCII genes and *Ciita* induced by FD treatment (Fig. 3G). Similarly, KEGG pathway enrichment of antigen processing and presentation upon the merged data was significantly suppressed after FD treatment (Fig. 3H). Furthermore, we extracted the merged list of DEGs and submitted to the ChEA (ChIP-X Enrichment Analysis) 2022 database of TF chromatin immunoprecipitation sequencing (ChIP-seq) data from BMDMs (*15*) for comparison. Down-regulated genes showed a similar profile to genes regulated by PU.1 and IRF8 and the HDAC-mediated repression complex proteins NCOR and silencing mediator of retinoid and thyroid hormone receptors (SMRT) (fig. S9F). Up-regulated genes correlated with nuclear factor erythroid 2–related factor 2 (NRF2) and PPARγ regulation (fig. S9F), highlighting the potential contribution of antioxidant genes to FD protection. We also observed a reduction in chromatin accessibility at *H2-Ab1*, *Ciita*, and *Ccl8* regions associated with the binding of PU.1 and acetylation of H3K27, an active transcription mark, from publicly available ChIP-seq datasets (*16*, *17*) (Fig. 3I and fig. S9G). Binding of PU.1 to the Ets motif in the *Ciita* promotor has been previously shown to directly regulate its transcription (*18*). In support, we also observed significant suppression of antigen processing and presentation within KEGG, while the PPAR signaling pathway was conversely enriched in FD-exposed BMDMs (fig. S9H), suggesting a potential upstream regulatory mechanism. Similarly, we examined BMDCs, which revealed comparable results for global ATAC-seq accessibility (fig. S10, A and B). DESeq2 analysis, however, demonstrated that BMDCs exposed to FD develop a unique epigenetic profile (fig. S10, C and D). Motif enrichment analysis also pointed to PU.1, IRF-related, and PU.1: IRF8 motifs to be present in the closed regions induced by FD exposure (fig. S10E). Chromatin accessibility at *Ciita* and *H2-Ab1* was also reduced in the region of H3K27Ac (*19*) (fig. S10F). Next, ATAC-seq and RNA-seq data were also integrated and showed a linearity similar to BMDMs, with MHCII-associated genes being epigenetically repressed (fig. S10G). Together, these findings identify epigenetic remodeling as a crucial mechanism of FD-dependent allergy prevention by reducing chromatin accessibility at genetic loci responsible for antigen presentation.

HDAC activity regulated by PPARγ signaling maintains MHCII suppression

Chromatin accessibility is tightly controlled by histone acetylation. In particular, acetylation on lysine-27 of histone H3 is an established marker of active transcription, and HDACs are important players to remove acetyl groups to regulate transcription (*20*, *21*). In line, Western blot analysis from nuclear extracts of BMDMs shows that

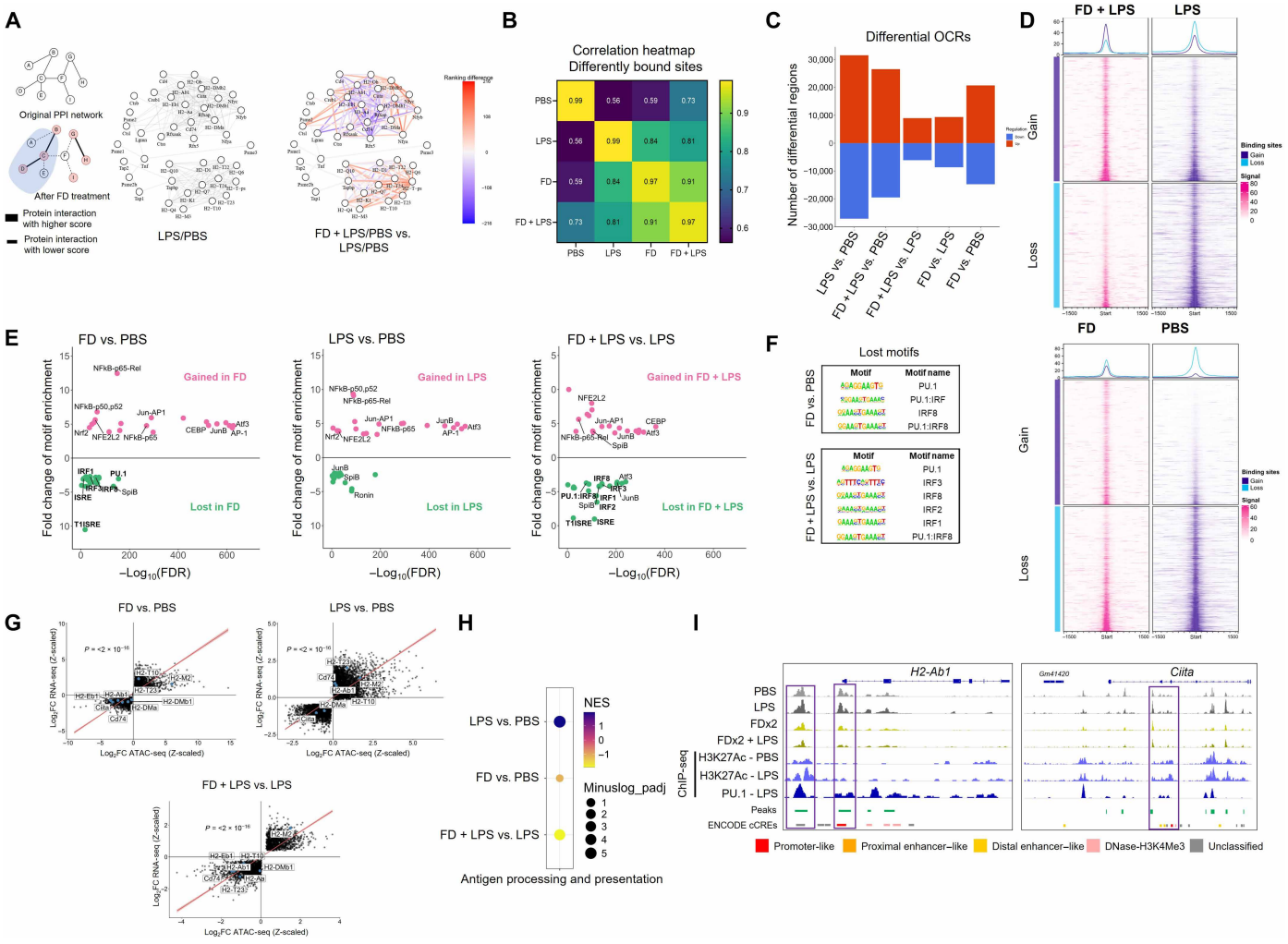

Fig. 3. ATAC-seq and RNA-seq integration in BMDMs identifies that MHCII gene chromatin closing is associated with reduced gene expression. (**A**) PPI networks derived from BMDM RNA-seq (LPS versus FD + LPS, PBS baseline). Modules were clustered by KEGG/Reactome terms; antigen presentation node shows altered interaction strength. (**B**) DESeq2 was used to normalize the counts between the samples and to generate comparisons for differential OCRs. Correlation heatmap from significantly differentially bound sites among groups. (**C**) A bar plot of the number of pairwise open or closed regions was generated from DESeq2 output. (**D**) Profile heatmap plots from FD + LPS versus LPS and FD versus PBS pairwise contrasts highlighting gained and loss bounding sites. (**E**) Motif enrichment analysis was performed using HOMER on significantly gained and lost peaks. Results plotted as fold change in enrichment compared to background. (**F**) Motifs related to PU.1 and IRFs found in lost accessibility regions comparing FD versus PBS and FD + LPS versus LPS are highlighted. (**G**) OCRs calculated using DESeq2 were integrated with significantly ($P < 0.05$) up- or down-regulated genes in bulk RNA-seq analysis, and genes that showed a modulation of at least $\log_2FC = 1.5$ between conditions were further filtered. A linear regression was traced using z-scaled $\log_2FC$ from RNA-seq DEGs and ATAC-seq significant differential OCRs. (**H**) GSEA on the integrated genes from pairwise comparisons, LPS versus PBS, FD versus PBS, and FD + LPS versus LPS, was performed. Antigen Processing and Presentation (mmu04612) KEGG pathway results are shown. (**I**) Tracks around *H2-Ab1* and *Ciita* genes from mm10 genome were visualized using IGV. H3K27Ac ChIP-seq tracks from PBS and LPS-stimulated BMDMs and PU.1 ChIP-seq in LPS-stimulated BMDMs were downloaded and incorporated. Regions where FD and FD + LPS show decreased peak heights in association to peaks from H3K27Ac and PU.1 were highlighted.

H3K27Ac is reduced by FD treatment (fig. S11A). Similarly, scRNA-seq analysis from FD-exposed mice displayed increased gene expression of multiple *Hdac* genes in MDMs (Fig. 4A), which was replicated ex vivo in BMDMs (Fig. 4B). Conversely, multiple histone acetyltransferase (HAT)–related genes like *Ep300* and *Crebbp* were down-regulated (Fig. 4B). Next, we investigated whether inhibition of HDACs during FD treatment could reverse repression of MHCII genes. Vorinostat, a pan-HDAC inhibitor, rescued the expression of *H2-Ab1* that was reduced by FD (Fig. 4C). Similarly, human leukocyte antigen–DR (HLA-DR) surface expression was rescued by vorinostat in human PBMC-derived BMDMs treated with FD extract (Fig. 4D). Furthermore, specific HDAC subtypes were inhibited using entinostat for class I and TMP195 for class IIa. Greatest rescue was obtained by blocking the class IIa HDACs, which include HDAC4, HDAC 5, HDAC 7, and HDAC9 (fig. S11B). The activity of HDAC enzymes is profoundly affected by the oxidation state of critical cysteine residues, reducing their deacetylase capacity (*22*). scRNA-seq reveals that multiple antioxidant enzyme genes are up-regulated following FD exposure in MDMs (Fig. 4E). In line, antioxidant genes were also up-regulated in BMDMs treated with FD ex vivo (Fig. 4F). To validate this, in an additional model of oxidative stress, RAS-selective lethal 3 (RSL-3)–mediated lipid peroxidation

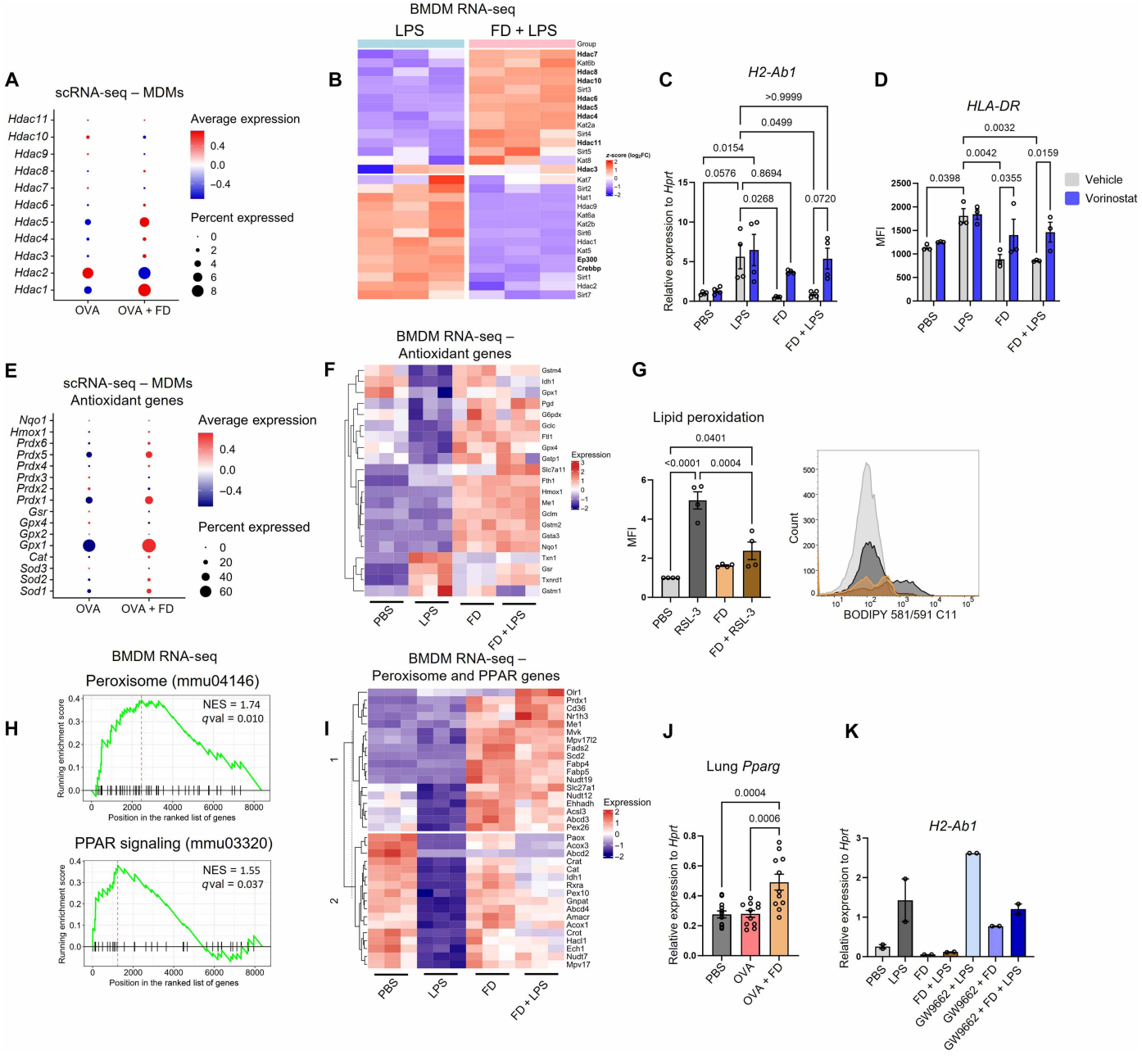

Fig. 4. FD-induced epigenetic regulation is dependent on HDAC activity. (**A**) Average gene expression from *Hdac* genes extracted from subset MDMs derived from scRNA-seq analysis comparing OVA and OVA + FD groups. (**B**) Normalized counts from HDAC and HAT genes, derived from BMDM RNA-seq analysis, were plotted as a heatmap and compared between LPS and FD + LPS groups. (**C**) The expression of *H2-Ab1* gene was assessed when pan-HDAC inhibitor vorinostat was added to media during FD exposure. (**D**) Vorinostat was also concomitantly added to FD in media from human monocyte–derived APCs, and HLA-DR MFI was measured via flow cytometry. (**E**) The average expression of antioxidant genes in MDMs, including the families of superoxide dismutase (*Sod1*, *Sod2*, and *Sod3*), catalase (*Cat*), glutathione peroxidase (*Gpx1*, *Gpx2*, and *Gpx4*) and reductase (*Gsr*), peroxiredoxin (*Prdx1–6*), oxidoreductase (*Nqo1*), and heme oxygenase (*Hmox1*), were plotted and compared between OVA and OVA + FD groups. (**F**) The main cellular antioxidant regulator Nfe2l2 target genes. Normalized gene expression was plotted in a heatmap comparing BMDMs in PBS, LPS, FD, and FD + LPS treatment groups. (**G**) Oxidative status of the BMDMs was assessed via lipid peroxidation assay in flow cytometry, using the sensor BODIPY 581/591 C11 fluorescein isothiocyanate/ phycoerythrin channels. Cells were pretreated with FD and exposed during 6 hours to the lipid peroxidation inducer RSL-3 (1 μM). (**H**) GSEA of FD + LPS versus LPS DEGs identified enrichment of KEGG terms Peroxisome (mmu04146) and PPAR signaling (mmu03320) in RNA-seq from BMDMs. (**I**) A heatmap was generated using normalized counts from the genes found to be significantly increased in Peroxisome and PPAR signaling terms in FD + LPS group. (**J**) *Pparg* gene expression was measured via RT-qPCR in OVA-exposed mouse lung homogenates. (**K**) The expression of *H2-Ab1* was assessed via RT-qPCR in BMDMs exposed to FD, where the selective PPARγ inhibitor GW9662 was concomitantly added. Results are plotted as means ± SEM, and difference between means were compared using one-way ANOVA followed by Tukey's post hoc test ($n = 2$ to 4).

was prevented by FD treatment, as measured by the BODIPY C11 peroxidation sensor (Fig. 4G). Similarly, genes related to lipid metabolism were increased following FD treatment (fig. S11C). A global regulator of antioxidant defense is the PPAR signaling pathway (*23*, *24*). Significantly, gene set enrichment analysis (GSEA) (Fig. 4H) and KEGG pathway (fig. S11D) analysis of FD-treated BMDMs indicated an enrichment of peroxisome and PPAR signaling with increased gene expression (Fig. 4I). In line, we observed increased gene expression of *Pparg* within lungs of FD-exposed mice (Fig. 4J). Last, blocking PPARγ signaling with GW9662 in BMDMs rescued the expression of *H2-Ab1* that was reduced by FD (Fig. 4K). Similarly, a PPARγ inhibition using the dual-allosteric inhibitor SR16832 (*25*) was able to reverse the FD-induced reduction of *Ccl8* expression in BMDMs (fig. S11E). KEGG pathway analysis also highlighted enrichment in metabolic pathways after FD exposure of BMDMs. In support, transcriptomics analysis revealed up-regulation of oxidative phosphorylation (fig. S11, D to F). These results suggest that FD shifts energy metabolism from glycolysis toward oxidative phosphorylation. Together, these data suggest that FD exposure induces epigenetic silencing of antigen presentation and eosinophil chemoattractant *Ccl8* expression, through a PPAR-regulated, HDAC-dependent axis in MDMs.

DISCUSSION

Here, we have explored the immunological basis for the beneficial effects of environment, using FD extract's protection against allergic lung inflammation, proposing mechanistic insight into how children raised in traditional farm environments exhibit long-lasting and efficient protection against allergic diseases, including asthma. Our results suggest that signaling triggered by FD, particularly MDMs that have migrated to the lungs, induces PPAR-mediated, HDAC-dependent epigenetic remodeling, which limits accessibility to the chemokine *Ccl8* and MHC class II–related genes. This reduces pathogenic eosinophil recruitment and local T cell activation and proliferation, respectively (fig. S11G), ultimately resulting in a blockade of the allergic inflammatory cascade.

CCL8 is a chemokine that has been previously demonstrated to play a critical role in inducing the initiation of allergic skin inflammation, via mobilization of eosinophils and interleukin-5–positive (IL-5$^+$) T_H2 cells to the site of inflammation (*8*). In addition, interfollicular CD169$^+$ macrophages have been shown to secrete CCL8 and attract allergy initiating CD301b$^+$ DCs to cutaneous draining lymph nodes, mediated via CCR8 receptor signaling (*26*). We demonstrate that MDM-derived CCL8 played an important role in mobilizing inflammatory eosinophils to the lungs in response to OVA challenge and generating AHR and mucus cell hyperplasia, which was abrogated following anti-CCL8 treatment.

The role that FD-induced, HDAC-mediated deacetylation plays on the suppression of *Ccl8* and MHCII gene expression was one the most notable findings of this study, particularly considering the increased recruitment of MDMs upon FD treatment. The exposome has been shown to play a determinant role through epigenetic modulation of immune cells in conferring susceptibility to chronic lung diseases, including asthma (*26*, *27*). Our findings expand this concept, highlighting that FD confers protection against disease by reducing H3K27 acetylation and increasing the expression of HDAC genes. Furthermore, pharmacological inhibition of HDACs using vorinostat and subtype-specific HDAC inhibitors rescued *H2-Ab1* expression in FD-exposed BMDMs. Modulation of HDAC activity using inhibitors has been shown to induce the transcription of MHC molecules and improve tumor immunogenicity (*28*–*30*). In the context of epithelial barrier function, HDAC inhibition has been reported to improve barrier integrity in patients with asthma (*31*). Consistent with previous findings showing a positive effect of FD on epithelial barrier function (*32*), FD treatment of 16HBEs also enhanced barrier integrity in our system (fig. S12, A and B). While our single-cell data indicate a potential reduction in the expression of some HDAC genes upon FD treatment, the role of HDACs likely depends on the specific cell type. Noteworthy, the observed epigenetic changes are reminiscent of trained immunity, a concept of long-term functional reprogramming of immune cells leading to an altered and persistent response upon a second challenge (*33*). This effect is clearly distinguishable from the LPS-induced tolerance as highlighted by the direct comparison of tolerizeable and nontolerizeable genes described by Foster *et al.* (*34*). While most of the expected tolerizeable genes are indeed suppressed by FD pretreatment, an additional set of genes, expected to be not LPS tolerizeable, conversely were tolerizeable by FD (fig. S13, A and B). PU.1 and IRFs are crucial regulators for MHCII gene expression via *Ciita* expression in response to inflammatory stimulation, especially binding to the pIV promoter (*11*). We observed that closed genomic regions in FD-exposed BMDMs and BMDCs are associated with motifs for TFs from these families. In particular, chromatin closing in the *Ciita* promoter was shown to be dependent on deacetylation via HDAC1/2 to compete for binding of RFX5 (*14*). IRF8 is also a crucial TF to induce differentiation of APCs, which is associated with enhanced antigen presentation (*12*, *13*).

In addition, the up-regulation of antioxidant genes following FD exposure suggests a potential link between oxidative stress regulation and epigenetic control. This is consistent with earlier studies showing HDAC activity to be profoundly reduced via oxidative modifications in the reactive oxygen species–rich asthma and COPD lungs, which lead to steroid insensitivity, since glucocorticoids use HDAC2 to suppress proinflammatory gene expression (*35*–*37*). FD treatment of BMDMs ex vivo and mouse lungs in vivo induced PPARγ signaling and the expression of multiple antioxidant genes, including the lipid peroxidation protector *Gpx4*. Notably, pharmacological inhibition of PPARγ reversed the suppression of *Ccl8* and MHCII genes, suggesting that FD-induced protection against allergy is mediated through PPARγ-dependent mechanisms. The role of PPARγ in immune regulation has been well established, with previous studies indicating that PPARγ activation can suppress proinflammatory gene expression and modulate macrophage function (*38*–*40*). Further work is required to pinpoint the sole contributing component of FD extract to the up-regulation of PPARγ. However, the HDAC-mediated epigenetic regulation downstream of PPARγ signaling in MDMs is crucial for the impaired expansion of antigen-specific T cells and reduced proinflammatory gene secretion, including the eosinophil attractor CCL8. A recent study from our group has demonstrated a presence of lipoproteins and lipocalins in FD extract, such as BOSd2 and OBP, which hauls a variety of long-chain fatty acids (LCFAs) as cargo (*41*). PPARγ is a receptor known to be triggered by LCFA and to induce profound immunoregulation (*42*). Moreover, PPARγ agonists have been shown to function as repressors of interferon-γ–induced *Ciita*, via direct binding to the promoter IV region (*43*). Ligand-bound PPARγ receptor can recruit HDACs to deacetylase and inhibit the expression of proinflammatory

genes via counteracting the nuclear export and proteasomal degradation of nuclear receptor corepressor 1 (NCoR1) (*44*–*46*), supporting our conclusions.

In summary, our study sheds light into the mechanistic basis for FD-induced prevention of allergic airway inflammation and provides insights into translational mechanisms of human asthma. Our data reveal that FD exposure operates through the recruitment of MDMs that secret reduced levels of CCL8. These MDMs are epigenetically modified via HDAC-dependent mechanisms to reduce the expression of MHCII genes, providing a suboptimal stimulus for antigen presentation to T cells. Furthermore, the interplay between HDAC activity, PPARγ signaling, and oxidative stress regulation underscores the multifaceted immunoregulatory effects of FD, linking to epigenetic control. These findings provide evidence into the crucial role that environmental factors play into determining individual progression to health or disease states.

MATERIALS AND METHODS

Human samples

PBMCs used for monocyte isolation were obtained from the blood of healthy volunteers (Blutspendedienst des Bayerischen Roten Kreuzes GmbH, München). Serum from the blood of healthy controls and asthmatic patients for enzyme-linked immunosorbent assay (ELISA) was obtained from the Pulmonary Research Institute at LungenClinic Grosshansdorf, after ethical approval from the Ethics Committee at the Medical Association of Schleswig Holstein, Bad Segeberg, Germany (AZ 115/19 I). All participants provided informed written consent.

Animals

B6.129S4-Ccr2[tm1Ifc]/J (no. 004999, the Jackson Laboratory), B6.129-*Tlr2*^{tm1Kir}/J (no. 004650, the Jackson Laboratory), C57BL/6 J (no. 632, Charles River Laboratories), and BALB/c (no. 028, Charles River Laboratories) age-matched female mice were used. Mice were housed under specific pathogen–free conditions, were maintained at a constant temperature (20° to 24°C) and humidity (45 to 65%) with a 12-hour light cycle, and were allowed food and water ad libitum. Mice were euthanized by terminal exsanguination following anesthetic or via cervical dislocation, according to the end application. All animal experiments were approved by the ethics committee for animal welfare of the local government for the administrative region of Upper Bavaria (Regierungspräsidium Oberbayern) and were conducted under strict governmental and international guidelines in accordance with EU Directive 2010/63/EU.

FD collection and processing

FD was collected as previously published (*3*, *41*). In short, FD was collected from a traditional European cow farm in Southern Germany. Dust was collected from the stables by sweeping settled dust from ledges, windowsills, and other, higher shelves (at least 1 m above ground) to obtain dry airborne dust. Dust batches were tested individually and exhibited notably consistent biochemical and functional properties over time; they were used interchangeably throughout the project. All samples were stored at −20°C before use.

Lung function

Mice were anesthetized with medetomidine–midazolam–fentanyl (MMF) for tracheotomy. A small incision was made below the larynx, and a metal canula was inserted. Respiratory system resistance (Rrs) and Newtonian resistance (Rn) were measured with a FlexiVent (Scireq) at increasing concentrations of methacholine. Twenty microliters of methacholine (0, 3, 6, 12, and 24 mg/ml) in phosphate-buffered saline (PBS) was administered using an Aeroneb ultrasonic nebulizer, followed by two deep inflations and Snapshot and QuickPrime-3 measurements. Lung function was analyzed with FlexiWare (Scireq). Rrs and Rn were normalized to the PBS values of each mouse individually.

Allergic airway inflammation model and FD administration

Animals were sensitized to OVA (Sigma-Aldrich, grade VI, no. A2512) on days 0, 7, and 14 by intraperitoneal injection of 10 μg of OVA emulsified in 1.0 mg of aluminum hydroxide (Aluminject; Pierce Chemical) and diluted to 200 μl with PBS. Subsequently, mice were challenged on days 26, 27, and 28 with intranasal administration of 100 μg of OVA (Sigma- Aldrich, grade V, no. A5503) diluted to 25 μl with PBS. Twenty-four hours after the last challenge, mice were deeply anesthetized in MMF, exsanguinated via the hepatic artery, and processed for downstream analysis.

FD extract was administered intranasally (25 μl) at a concentration of 32 mg/ml, resulting in a dose of 800 μg per application. A total of 12 administrations were carried out on days 0, 2, 5, 7, 9, 12, 14, 16, 19, 21, 23, and 26. A schematic of the full experimental protocol is provided in fig. S1A. The dose and administration times were chosen on the basis of preliminary studies optimizing concentration and timing (fig. S14), where the 800-μg dose demonstrated the most effective protective outcome, particularly the most significant reduction in BAL eosinophilia.

Anti-CCL8 antibody treatment

Anti-CCL8 antibody (5 μg) (BioLegend, 536902) or rat IgG2bκ isotype control (BioLegend, 400601) was administered intraperitoneally 6 hours before intranasal OVA challenges in WT BALB/c mice that were previously sensitized. Twenty-four hours after the last challenge, mice were deeply anesthetized in MMF, exsanguinated via the hepatic artery, and processed for downstream analysis.

BAL processing

Lungs were lavaged three times with 0.5 ml of PBS containing protease inhibitors. BAL was centrifuged for 20 min at 1500 rpm, the supernatant was snap frozen and stored at −80°C for future analysis, and the cell pellet was resuspended in 1 ml of cell growth medium containing 10% fetal bovine serum (FBS). Total counts were performed using a hematocytometer, and 50,000 cells were used to prepare cytospin slides. Differential cell counts were performed using morphological criteria on May-Grünwald-Giemsa–stained cytospins (200 cells per sample).

Lung tissue processing and histology

After BAL collection, animals were exsanguinated via inferior vena cava section, and blood was collected. Serum was isolated after centrifuging blood samples at 4°C for 15 min at 3500*g* and stored at −80°C for future use. Right lungs were tied, and the middle lobe was flash frozen and stored at −80°C for later applications. The upper and lower lobes were isolated, and single-cell suspension was prepared for flow cytometry analysis, as described below. The left lung was perfused via the right ventricle with heparin containing cold PBS until blood was removed. The lung was then filled via the tracheas with 4% paraformaldehyde (PFA) during 15 min at a pressure

height of 25 cm, tied, and kept overnight in 4% PFA at 4°C until washing and storage in PBS the next day. The lungs were embedded in paraffin using conventional histological preparation, and 4-µm-thick sections were prepared using a microtome.

Lung IHC, PAS, and hematoxylin and eosin staining

Three-micrometer-thick sections from mouse left lung were deparaffinized in xylene and rehydrated before treatment with 1.8% (v/v) H_2O_2 solution (Sigma-Aldrich) to block endogenous peroxidase. Heat-induced epitope retrieval was performed in heat-induced epitope retrieval citrate (HIER) buffer (pH 6.0, Zytomed Systems) in a decloaking chamber (Biocare Medical). To inhibit nonspecific binding of antibodies, sections were treated with rodent blocking buffer (Biocare Medical). After overnight incubation with a primary antibody against CD11b (ab33357, Abcam), CD11c (ab21979, Abcam), and CD68 (ab125212, Abcam) at 4°C, sections were incubated with an alkaline phosphatase (AP)– or horseradish peroxidase (HRP)–conjugated secondary antibody (Rabbit-on-Rodent AP-Polymer catalog no. RMR625H, Rabbit-on-Rodent HRP-Polymer catalog no. RMR622H, and Mouse-on-Mouse AP-Polymer catalog no. MM62-4H, all Biocare Medical) at room temperature (RT) for 1 hour. Signals were amplified by adding chromogen substrate Vulcan fast red or 3,3′-diaminobenzidine (Biocare Medical), respectively. Sections were counterstained with hematoxylin (Sigma-Aldrich) and dehydrated in xylene and mounted with Entellan (Merck). PAS staining and hematoxylin and eosin staining were performed on deparaffinized sections using conventional histological processing. Histology images were acquired using a Zeiss Mirax Microimaging slide scanner running MIRAXDESK v1.12.25.1 and a Mirax viewer v1.12.22.0 software (Zeiss, 3D Histech). To determine the number of positively stained cells, eosinophils, or PAS^+ goblet cells across the lung, a frame grid was superimposed on lung section images taken with the ×40 objective, and positive cells were counted across at least 20 random fields per lung, as previously published (*47*).

Flow cytometry

Two lobes of the right lung were processed using the gentleMACS Dissociator according to the Miltenyi Lung Dissociation Kit (Miltenyi Biotec, no. 130-095-927) protocol. Following the dissociation, red blood cell lysis was performed for 2 min at RT. After the red blood cell lysis, the cells were counted for the following FACS staining. The cells were first incubated with anti-CD16/32 blocking antibody (Invitrogen, no. 23348094) and then stained with Live/Dead cell viability dye (Zombie Aqua or Fixable Viability Stain 620) and antibodies for surface markers (table S1). The cells were fixed and permeabilized using the Foxp3/Transcription Factor Staining Buffer Set (Miltenyi Biotec, 130-093-142) and subsequently stained with intracellular markers (table S1). The samples were analyzed using the BD FACSymphony A1 Cell Analyzer running BD FACSDiva v8. Flow cytometry data were analyzed using FlowJo v10.

Western blot

Protein was extracted with radioimmunoprecipitation assay buffer containing Halt Protease Inhibitor Cocktail (Thermo Fisher Scientific, no. 78430). The protein concentration was determined with a Pierce bicinchoninic acid (BCA) assay kit (Thermo Fisher Scientific, no. A55865), and samples were diluted in Laemmli buffer (Bio-Rad, no. 1610747) containing 0.5% β-mercaptoethanol to a final protein concentration of 0.5 µg/µl. Ten microliters of sample was loaded onto a 12.5% SDS gel and run at 80 V for 20 min followed by 1.5 hours at 120 V. The separated proteins were then transferred to a polyvinylidene difluoride membrane using a fully wet transfer system at 80 V for 70 min. The membrane was blocked for 30 min on RT and then incubated with primary antibody overnight at 4°C. After washing 3× in phosphate-buffered saline with Tween-20 (PBST), the secondary antibody conjugated with HRP was incubated for 1.5 hours at RT. Following 3× washing in PBST, SuperSignal West Femto (Thermo Fisher Scientific, no. 1859023) was added, and signal intensity was measured with ChemiDoc (Bio-Rad).

RNA isolation and cDNA synthesis

RNA from BMDMs and BMDCs was isolated with an RNeasy Plus Mini Kit (Qiagen, no. 74136) according to the manufacturer's protocol. In short, cells were lysed, DNA was removed with genomic DNA columns, and RNA was purified with an RNA binding column and multiple wash steps. RNA was eluted with 30 µl of ribonuclease-free dH_2O. RNA concentration was measured with a NanoDrop Spectrophotometer (Thermo Fisher Scientific). For cDNA synthesis, RNA concentration was equalized between samples in separate tubes at 10 µl. RNA was incubated at 60°C for 5 min and cooled down for 5 min on ice. High-Capacity RNA-to-cDNA mix (10 µl) (Applied Biosystems, no. 4387406) was added, and the cDNA was amplified in a polymerase chain reaction (PCR) cycler (Eppendorf Mastercycler Nexus Gradient) according to the manufacturer's protocol.

Quantitative PCR

Gene expression was measured with a QuantStudio3 (Applied Biosystems). Quantitative PCRs (qPCRs) were performed with PowerUP SYBR mix (Applied Biosystems, no. A25743) in MicroAmp 96-well plates (Applied Biosystems, no. 4306737). Forward and reverse primers were synthesized by Eurofins and used at a concentration of 10 pmol/µl. Primers were designed using Primer-BLAST software (www.ncbi.nlm.nih.gov/tools/primer-blast/) or obtained from PrimerBank (https://pga.mgh.harvard.edu/primerbank/). Primer sequences can be found in table S2. Relative expression of each gene was calculated relative to the housekeeping gene *HPRT1* or *Hprt1* as $2^{-\Delta Ct}$.

Enzyme-linked immunosorbent assay

Mouse CCL8 (BioLegend, no. 446904), human CCL8 (BioLegend, no. 442204), OVA-specific IgE (Chondrex, no. 3004), and OVA-specific IgG1 (Chondrex, no. 3013) were used according to the supplier's protocols. Serum was diluted 1:500 and bronchoalveolar lavage 1:5 in assay diluent. Samples were measured in duplicate, and the concentration was calculated by interpolating a standard curve.

Ccl8 promoter analysis

To identify potential regulators of *Ccl8*, we extracted the gene promoter region [−2000 to +500 base pairs (bp)] from the mm10 genome. Next, we inserted these genomic regions into CistromeDB Toolkit (http://dbtoolkit.cistrome.org/) and extracted a list of potential binding TFs, based on published datasets.

BMDM and BMDC generation

BMDM generation

Bone marrow was isolated from C57BL/6 J mice and cultured at a density of 3×10^6 bone marrow cells in 3 ml of complete medium (RPMI 1640, 10% heat-inactivated fetal calf serum, penicillin,

streptomycin, and 2-mercaptoethanol) supplemented with macrophage colony-stimulating factor (M-CSF) (20 ng/ml) (ImmunoTools no. 12343115) in six-well plates. On days 3 and 6, half of the medium was removed and replaced with fresh medium containing M-CSF (40 ng/ml). On day 7, total medium was changed and replaced with medium containing M-CSF (10 ng/ml). Macrophages were used for experiments from day 8 onward. BMDM differentiation efficacy was assessed by flow cytometry staining for CD11b and F4/80, reaching 90 to 95% purity.

BMDC generation

Bone marrow was isolated from C57BL/6 J mice and cultured at a density of 4×10^6 bone marrow cells per petri dish in 10 ml of complete medium (RPMI 1640, 10% heat-inactivated fetal calf serum, penicillin, streptomycin, and 2-mercaptoethanol) supplemented with granulocyte-macrophage colony-stimulating factor (GM-CSF) (20 ng/ml) (ImmunoTools no. 12343127). On day 3, 10 ml of fresh medium containing GM-CSF (20 ng/ml) was added to each petri dish. On day 6, half of the medium was removed and replaced with fresh medium containing GM-CSF (20 ng/ml). On days 8 and 10, half of the medium was again removed and replaced with fresh medium containing GM-CSF (10 ng/ml). On day 12, nonadherent cells and loosely adherent cells were harvested by gentle washing with PBS and pooled cells used for further experiments.

BMDM and BMDC OT-II coculture

BMDMs and BMDCs were differentiated as described above and treated with FD (100 μg/ml) or PBS twice over a 24-hour period. Following treatment, BMDMs were incubated with LPS (10 ng/ml) for 6 hours, and BMDCs were incubated overnight with LPS (10 ng/ml). Both cell types were then pulsed with OVA peptides 323 to 339 (Sigma-Aldrich, no. O1641) for 3 hours. In parallel, naïve T cells were isolated from OT-II mice [B6.Cg-Tg(TcraTcrb)425Cbn/J] (the Jackson Laboratory, no. 004194) using the Naïve CD4+ T Cell Isolation Kit (Miltenyi, no. 130-104-453) and stained with CellTrace Violet (Thermo Fisher Scientific, no. C34571). A total of 100,000 T cells were plated in a 96-well plate in 100 μl of medium, and 50,000 BMDMs or BMDCs in 100 μl were added. After 4 days of coculture, T cells were restimulated with eBioscience Cell Stimulation Cocktail (Thermo Fisher Scientific, no. 00-4970-93) for 5 hours, and the mean fluorescence intensity (MFI) of the proliferation dye was measured by flow cytometry (fig. S15). The proliferation index was calculated using the formula (1/MFI) *1000.

Lipid peroxidation

BMDMs were treated with FD, LPS, or RSL-3 (Cayman Chemical, 1 μM) and subsequently incubated with BODIPY 581/591 C11 (Thermo Fisher Scientific, D3861) for 30 min at 37°C, 5% CO_2. Cells were washed with PBS, trypsinized, and transferred to flow cytometry tubes. A total of 20,000 events were recorded and gated for single cells. MFI of phycoerythrin (total amount of dye uptaken) and fluorescein isothiocyanate (oxidized dye) were measured.

The mouse PPI network construction

Curated protein-protein interaction (PPI) data for mouse and human were obtained from the IntAct database as of March 2023 (*48*). We selected high-confidence PPIs that were supported by at least two independent evidences, i.e., publications or experimental experiments, to ensure reliability (*49*). The initial mouse PPI network comprised 2326 interactions among 2150 proteins, while the human network consisted of 13,262 proteins linked by 96,635 interactions. To overcome the limited coverage of the mouse PPI network, we mapped human high-quality interactions to mouse orthologs (interolog mapping) (*50*). For this, human-mouse ortholog pairs were retrieved from the Ensembl database (May 2023). Human PPIs, where both human partners had a one-to-one ortholog, were mapped to the corresponding mouse proteins. After applying this ortholog filter on high-quality IntAct interactions, 68,308 interactions among 11,049 proteins could be transferred to mouse. To further enhance the mouse PPI network, we integrated high-quality high-throughput human PPI data from the Human Reference Interactome and BioPlex 3 datasets (*51*, *52*). After ortholog matching and merging of all datasets, we obtained a network of 140,186 unique interactions (edges) among 13,663 mouse proteins (nodes).

For functional network analysis, we generated modules using several complementary approaches. Functional KEGG pathway modules were parsed using KEGGREST v1.37.0 and the KEGGGraph v1.66.0 (*53*) R packages, while REACTOME pathway modules were directly downloaded from Reactome (September 2023) (*54*, *55*). Network topology-based modules were constructed using the linkcomm (*55*) R package following the link community algorithm (*56*). Last, to cover the full network, centroid "modules" were defined by selecting each center protein together with its immediate (one-hop) neighbors from the generated mouse PPI network.

To identify the interaction partners that are coherently regulated in specific conditions, suggesting shared functions, we calculated conditional PPI scores on the basis of the transcripts per million (TPM) values of the two interaction partners

$$\text{Conditional PPI score} = \frac{\text{TPM}_A^1}{\text{TPM}_A^2} \times \frac{\text{TPM}_B^1}{\text{TPM}_B^2} \times \cos\left[\left(\text{TPM}_A^1, \text{TPM}_B^1\right), \left(\text{TPM}_A^2, \text{TPM}_B^2\right)\right]$$

The cosine similarity $\cos\left[\left(\text{TPM}_A^1, \text{TPM}_B^1\right), \left(\text{TPM}_A^2, \text{TPM}_B^2\right)\right]$, which assesses similarity in the expression of genes A and B between two conditions, was computed using the TPM values of gene A in conditions 1 and 2 and gene B in conditions 1 and 2. The fold changes of the interaction partners A and B and of $\frac{\text{TPM}_A^1}{\text{TPM}_A^2}$ and $\frac{\text{TPM}_B^1}{\text{TPM}_B^2}$ were used to scale the conditional PPI scores such that larger changes in expression are weighed stronger. In essence, the conditional PPI score integrates both the magnitude of changes in gene expression levels and the directional relationship of the expression profiles across the two conditions. A higher PPI score suggests a stronger, more coordinated change in expression between the two genes, which may indicate functional relevance of the interaction in that condition. Conditional PPI scores were calculated for all interaction pairs for the following comparisons: (i) LPS-stimulated DC or macrophage versus control and (ii) LPS-stimulated DC or macrophage after two doses of cow dust pretreatment versus cells receiving two doses of cow dust pretreatment alone. To identify which of the above-defined modules show coordinated regulation, we calculated a ranking difference and the sum of ranking difference (SRD) (*57*) for each module: The ranking difference quantifies the relative change of each individual PPI between two conditions; a strong positive ranking difference indicates that the PPI score was clearly higher in condition 2 compared with condition 1. The SRD for a module reflects the aggregate difference in conditional PPI scores across conditions and is computed as the sum of the ranking differences for each

individual PPI when comparing the two conditions. This integrated measure captures the overall shift in interaction profiles within the module. A null distribution was generated using 1000 random permutations, and the observed SRD values were compared with this null distribution to identify statistically significant modules.

Bulk RNA-seq from BMDM and BMDC

RNA (1 μg) isolated, as previously described, from BMDMs and BMDCs was sent to Active Motif (Carlsbad, CA) for bulk RNA-seq analysis. Illumina raw sequencing reads were aligned using STAR algorithm (vSTAR_2.6.1d) via default settings. After obtaining the gene table containing the fragment counts of genes, differential analyses to identify statistically significant differential genes were performed using DESeq2. Differential genes are filtered at a threshold of 0.1 (or 10%) false discovery rate and $\log_2$FC <> 0.5. GSEA on filtered and merged genes was performed using the gseKEGG function from KEGG.db package.

Assay for transposase-accessible chromatin using sequencing

Approximately 100,000 BMDM and BMDCs were sent to Active Motif (Carlsbad, CA) for ATAC-seq analysis, after cryopreserving the cells as described in the ATAC-seq sample preparation guidelines supplied by the company. Briefly, barcoded libraries were sequenced 42-bp paired-end on NextSeq 500 (Illumina). The paired-end 42-bp sequencing reads (PE42) were mapped to the genome using the Burrows–Wheeler aligner (BWA) algorithm with default settings. Only reads that pass Illumina's purity filter, align with no more than two mismatches, and map uniquely to the genome were used in the subsequent analysis. In addition, duplicate reads ("PCR duplicates") are removed. Genomic regions with high levels of transposition/tagging events were determined using the MACS3 narrow peak-calling algorithm (*58*). Peaks were annotated using CheepSeeker version 1.42.0 and *M. musculus* mm10 University of California, Santa Cruz (UCSC) transcript database (TxDb.Mmusculus.UCSC.mm10.knownGene) as reference. DiffBind version 3.16.0 was used to determine differential OCRs between samples. The ATAC-seq tracks were visualized in the UCSC Genome Browser (https://genome.ucsc.edu/) and IGV 2.17.2 (IGV: Integrative Genomics Viewer). For motif enrichment analysis, HOMER motif discovery and analysis v5.1 was used (findMotifsGenome.pl) on the 200-bp sequence centered around the midpoint of the differential region (+100 bp, −100 bp).

Merging between differentially OCRs with differentially expressed transcripts via RNA-seq was performed via merging results by the official gene symbol and subsequent *P* value filtering ($P < 0.05$). The $\log_2$FCs were z-scaled, and results were plotted. A linear regression shows the correlation of the two distributions. GSEA on filtered and merged genes was performed using the gseaKEGG function from KEGG.db package.

PBMC monocyte isolation and stimulation

For PBMC isolation, buffy coat blood was diluted in PBS + 2% FBS and overlaid on a density gradient medium (Histopaque-1077, Sigma-Aldrich, no. 10771) followed by centrifugation at 800*g*, 25 min without break. After centrifugation, an interface layer of PBMC was collected and washed twice with PBS followed by centrifugation at 800*g* and 400*g*, for 10 min to remove platelets. Cells were resuspended in PBS and counted by trypan blue staining, manually using a hemocytometer. PBMC monocytes were isolated by adherence on a cell culture plate using monocyte attachment medium (PromoCell, C-28051) according to the manufacturer's instructions. Approximately 1×10^6 monocytes in six-well culture plates were seeded. Adherent monocytes were cultured in RPMI 1640 medium with L-glutamine (containing 10% FBS, 0.1 mM nonessential amino acids, 1% penicillin, and 1% streptomycin) in a humidified atmosphere and stimulated with FD extract (100 μg/ml) for 48 hours followed by 6-hour stimulation with 1 μg of LPS. Afterward, samples were processed for ELISA and qPCR.

Monocyte-derived APCs were cultured in a complete medium supplemented with GM-CSF (40 ng/ml) (STEMCELL Technologies) for 8 days and IL-4 (20 ng/ml) (PromoKine, Heidelberg, Germany) for 5 days. On the sixth day, the culture was further supplemented with IL-1β (50 ng/ml) (StemCell) and tumor necrosis factor–α (50 ng/ml) (Biotechne, R&D Systems, Minneapolis, MN, USA).

Transepithelial electrical resistance assay

16HBE cells (a human bronchial epithelial cell line) were seeded onto 0.4-μm-pore Transwell inserts (a semipermeable membrane) at a confluent density. The cells were allowed to form a monolayer before treatment. Following the establishment of a confluent monolayer, cells were treated with FD (100 μg/ml) and LPS (1 μg/ml). Transepithelial electrical resistance (TEER) measurements were taken at 12, 24, and 48 hours posttreatment. TEER was quantified by measuring the electrical resistance across the confluent cell monolayer using a dedicated voltohmmeter. Electrodes were placed in the apical and basolateral compartments, separated by the cell layer. An alternating current (ac) was applied, and the resulting resistance R was recorded and calculated on the basis of Ohm's law ($R = V/I$), where V is voltage and I is current. TEER values directly reflect the electrical resistance across the cellular barrier, which is an established indicator of tight junction strength and overall barrier integrity.

Adoptive transfer

BMDMs and BMDCs were cultured as described above and treated with PBS, FD, or vorinostat (HY-102211, MedChemExpress, 1 μM) pretreatment during 48 hours. After this time, these cells were pulsed with OVA (100 μg/ml) (Sigma-Aldrich, grade VI, no. A2512). Antigen surface loading was confirmed using OVA–Alexa Fluor 555 (Thermo Fisher Scientific, O34782) conjugate via flow cytometry.

After this, cells were washed in PBS, counted, and stained in PKH26 (Thermo Fisher Scientific, no. PKH26GL) solution during 30 min, and 1×10^6 cells were resuspended in 50 μl of culture medium and kept on ice until transfer. Mice were deeply anesthetized using MMF and had a cannula inserted into their trachea. After the transfer of 1×10^6 cells, the mice were rested for 7 days, before three daily challenges with intranasal administration of 100 μg of OVA (Sigma-Aldrich, grade V, no. A5503) diluted to 25 μl with PBS. Twenty-four hours after the last challenge, mice were deeply anesthetized in MMF, exsanguinated via the hepatic artery, and processed for downstream analysis.

Single-cell RNA sequencing

Murine lobes were removed, minced, and digested for 20 to 30 min at 37°C in an enzymatic mix containing dispase (50 caseinolytic U/ml), collagenase (2 mg/ml), elastase (1 mg/ml), and deoxyribonuclease (30 μg/ml). Single cells were harvested by straining through a 70-μm strainer. After centrifugation at 300*g* for 5 min, single cells were taken up in 1 ml of PBS (with 10% fetal calf serum), counted,

and critically assessed for single-cell separation and overall cell viability. Cells were aliquoted in PBS supplemented with 0.04% of bovine serum albumin at a final concentration of 100 cells/μl.

Droplet sequencing (Drop-seq) experiments were performed according to the original protocol (*59*). Briefly, single cells (100/μl) were coencapsulated in droplets with barcoded beads (120/μl; ChemGenes Corporation, Wilmington, MA) at rates of 4000 μl/hour. Droplet emulsions were collected for 10 to 20 min per each before droplet breakage by perfluorooctanol (Sigma-Aldrich). After breakage, beads were harvested, and the hybridized mRNA transcripts were reverse transcribed (Maxima RT, Thermo Fisher Scientific). Unused primers were removed by the addition of exonuclease I (New England Biolabs), following which, beads were washed, counted, and aliquoted for preamplification (2000 beads per reaction, equals ~100 cells per reaction) with 12 PCR cycles. For each sample, 1 ng of preamplified cDNA from an estimated 1000 cells was tagmented by Nextera XT (Illumina) with a custom P5 primer (Integrated DNA Technologies). Single-cell libraries were sequenced in a 100-bp paired-end run on the Illumina HiSeq 4000 using 0.2 nM denatured sample and 5% PhiX spike-in.

scRNA-seq and data analysis

Following sequencing, the generation of count matrices was performed by using the Drop-seq core computational pipeline. The processing of next-generation sequencing reads of the scRNA-seq data was performed as previously described (*59*). Briefly, the Drop-seq computational pipeline was used (version 2.3.0, STAR version 2.5.3a) for the alignment of reads to the mm10 reference genome (provided by the Drop-seq group, GSE63269). For barcode filtering, we excluded barcodes with less than 200 detected genes.

During preprocessing, we assessed the quality of our libraries and applied suitable filter criteria motivated by previously described best practices (*60*) with slight adjustments. We kept the top barcodes based on unique molecular identifier (UMI) count per cell, guided by the number of estimated cells per sample. After exploration of UMI counts and genes per cell for the combined count matrices, we retained barcodes with count numbers in the range of 400 to 6000 counts per cell and genes detected in at least three cells. A high proportion (>20%) of transcript counts derived from mitochondria-encoded genes may indicate low cell quality, and we removed such unqualified cells. The expression matrices were normalized using scran's size factor–based approach and log-transformed via scanpy's pp.log1p() function. In an additional step to mitigate the effects of unwanted sources of cell-to-cell variation, we regressed out the number of UMI counts and cell cycle scores for each cell. Genes variable in at least four samples were used as input for PCA. Clustering was performed via scanpy's Louvain method at resolution 2, and cell types were manually annotated by using known marker genes. Downstream analyses were performed on converted Seurat object using Seurat version 5.1.0 on RStudio 2023.09.1+494 running R version 4.3.1. Graphs and aesthetics were performed using ggplot2 version 3.5.1 or scCustomize version 2.1.2.

Statistics

Results are presented as mean values ± SEM, with sample size indicated in the figure legend. One-way or two-way analysis of variance (ANOVA) following Tukey posttest was used for all studies with more than two groups. For comparisons between two groups, unpaired two-tailed Student's *t* test or Mann-Whitney *U* test was applied, according to sample distribution. *P* values less than 0.05 were considered significant. Analyses were conducted using GraphPad Prism 10 (GraphPad Software).

Supplementary Materials

This PDF file includes:

Figs. S1 to S15
Tables S1 to S3

REFERENCES

1. M. W. Pijnenburg, L. Fleming, Advances in understanding and reducing the burden of severe asthma in children. *Lancet Respir. Med.* **8**, 032–1044 (2020).
2. K. Mortimer, M. Lesosky, L. García-Marcos, M. I. Asher, N. Pearce, E. Ellwood, K. Bissell, A. El Sony, P. Ellwood, G. B. Marks, A. Martínez-Torres, E. Morales, V. Perez-Fernandez, S. Robertson, C. E. Rutter, R. J. Silverwood, D. P. Strachan, C. Y. Chiang, R. Masekela, D. P. Strachan, M. Urrutia Pereira, G. A. Ajeagah, M. E. Soto-Martínez, K. Priftis, J. Sanchez, S. K. Kochar, M. Singh, N. Singh, N. Sit, T. U. Sukumaran, S. Awasthi, P. A. Mahesh, S. Sinha, M. Barne, M. Tavakol, N. Behniafard, S. A. Alomary, I. Bucaliu-Ismajli, L. Hana-Lleshi, V. Gashi, X. Kurhasani, B. Gacaferri-Lumezi, L. N. Ahmetaj, V. Lokaj-Berisha, M. G. Sanchez Coronel, G. Ochoa-Lopez, R. García-Almaráz, J. A. Sacre Hazouri, M. D. J. Ambriz-Moreno, J. V. Mérida-Palacio, O. J. Saucedo-Ramirez, L. O. Hernández-Mondragón, A. Arias-Cruz, C. A. Jiménez González, A. J. Escalante-Dominguez, F. J. Linares-Zapién, E. M. Navarrete-Rodriguez, A. G. Falade, G. Brożek, K. Kyzmicheva, K. Yeh, S. Chinratanapisit, D. Solé, M. E. Soto-Quirós, V. Singh, W. A. Althagafi, B. E. Del Río Navarro, P. Vichyanond, The burden of asthma, hay fever and eczema in adults in 17 countries: GAN phase I study. *Eur. Respir. J.* **60**, 2102865 (2022).
3. M. M. Stein, C. L. Hrusch, J. Gozdz, C. Igartua, V. Pivniouk, S. E. Murray, J. G. Ledford, M. Marques Dos Santos, R. L. Anderson, N. Metwali, J. W. Neilson, R. M. Maier, J. A. Gilbert, M. Holbreich, P. S. Thorne, F. D. Martinez, E. von Mutius, D. Vercelli, C. Ober, A. I. Sperling, Innate immunity and asthma risk in amish and hutterite farm children. *N. Engl. J. Med.* **375**, 411–421 (2016).
4. H. Lim, Y. U. Kim, K. Yun, S. M. Drouin, Y. Chung, Distinct regulation of Th2 and Th17 responses to allergens by pulmonary antigen presenting cells in vivo. *Immunol. Lett.* **156**, 140–148 (2013).
5. H. Hammad, B. N. Lambrecht, The basic immunology of asthma. *Cell* **184**, 2521–2522 (2021).
6. M. J. Ege, M. Mayer, A.-C. Normand, J. Genuneit, W. O. C. M. Cookson, D. Phil, C. Braun-Fahrländer, D. Heederik, R. Piarroux, E. Von Mutius, Exposure to environmental microorganisms and childhood asthma. *N. Engl. J. Med.* **364**, 701–709 (2011).
7. P. V. Kirjavainen, A. M. Karvonen, R. I. Adams, M. Täubel, M. Roponen, P. Tuoresmäki, G. Loss, B. Jayaprakash, M. Depner, M. J. Ege, H. Renz, P. I. Pfefferle, B. Schaub, R. Lauener, A. Hyvärinen, R. Knight, D. J. J. Heederik, E. von Mutius, J. Pekkanen, Farm-like indoor microbiota in non-farm homes protects children from asthma development. *Nat. Med.* **25**, 1089–1095 (2019).
8. S. A. Islam, D. S. Chang, R. A. Colvin, M. H. Byrne, M. L. McCully, B. Moser, S. A. Lira, I. F. Charo, A. D. Luster, Mouse CCL8, a CCR8 agonist, promotes atopic dermatitis by recruiting IL-5^{+} T_H2 cells. *Nat. Immunol.* **12**, 167–177 (2011).
9. R. Zheng, C. Wan, S. Mei, Q. Qin, Q. Wu, H. Sun, C. H. Chen, M. Brown, X. Zhang, C. A. Meyer, X. S. Liu, Cistrome data browser: Expanded datasets and new tools for gene regulatory analysis. *Nucleic Acids Res.* **47**, D729–D735 (2019).
10. S. Heinz, C. Benner, N. Spann, E. Bertolino, Y. C. Lin, P. Laslo, J. X. Cheng, C. Murre, H. Singh, C. K. Glass, Simple combinations of lineage-determining transcription factors prime cis-regulatory elements required for macrophage and B cell identities. *Mol. Cell* **38**, 576–589 (2010).
11. A. Muhlethaler-Mottet, L. A. Otten, V. Steimle, B. Mach, Expression of MHC class II molecules in different cellular and functional compartments is controlled by differential usage of multiple promoters of the transactivator CIITA expression. *EMBO J.* **16**, 2851–2860 (1997).
12. M. A. Smith, G. Wright, J. Wu, P. Tailor, K. Ozato, X. Chen, S. Wei, J. F. Piskurich, J. P. Y. Ting, K. L. Wright, Positive regulatory domain I (PRDM1) and IRF8/PU.1 counter-regulate MHC class II transactivator (CIITA) expression during dendritic cell maturation. *J. Biol. Chem.* **286**, 7893–7904 (2011).
13. R. K. Pai, D. Askew, W. H. Boom, C. V. Harding, Regulation of class II MHC expression in APCs: Roles of types I, III, and IV class II transactivator. *J. Immunol.* **169**, 1326–1333 (2002).
14. X. Kong, M. Fang, P. Li, F. Fang, Y. Xu, HDAC2 deacetylates class II transactivator and suppresses its activity in macrophages and smooth muscle cells. *J. Mol. Cell Cardiol.* **46**, 292–299 (2009).
15. A. B. Keenan, D. Torre, A. Lachmann, A. K. Leong, M. L. Wojciechowicz, V. Utti, K. M. Jagodnik, E. Kropiwnicki, Z. Wang, A. Ma'ayan, ChEA3: Transcription factor

enrichment analysis by orthogonal omics integration. *Nucleic Acids Res.* **47**, W212–W224 (2019).
16. F. Gualdrini, S. Polletti, M. Simonatto, E. Prosperini, F. Pileri, G. Natoli, H3K9 trimethylation in active chromatin restricts the usage of functional CTCF sites in SINE B2 repeats. *Genes Dev.* **36**, 414–432 (2022).
17. H. C. B. Nguyen, M. Adlanmerini, A. K. Hauck, M. A. Lazar, Dichotomous engagement of HDAC3 activity governs inflammatory responses. *Nature* **584**, 286–290 (2020).
18. M. Ryosuke, K. Kazumi, N. Nobuhiro, H. Mutsuko, M. Keiko, O. Ko, O. Hideoki, Y. Takuya, N. Chiharu, Role of PU.1 in MHC class II expression via CIITA transcription in plasmacytoid dendritic cells. *PLOS ONE* **11**, e0154094 (2016).
19. B. Yang, S. Kim, W. J. Jung, K. Kim, S. Kim, Y. J. Kim, T. G. Kim, E. C. Lee, J. S. Joo, C. G. Park, S. Oh, K. H. Yoo, H. P. Kim, CTCF controls three-dimensional enhancer network underlying the inflammatory response of bone marrow-derived dendritic cells. *Nat. Commun.* **14**, 1277 (2023).
20. A. J. Bannister, T. Kouzarides, Regulation of chromatin by histone modifications. *Cell Res.* **21**, 381–395 (2011).
21. Y. Chen, R. Liang, Y. Li, L. Jiang, D. Ma, Q. Luo, G. Song, Chromatin accessibility: Biological functions, molecular mechanisms and therapeutic application. *Signal Transduct. Target Ther.* **9**, 340 (2024).
22. P. J. Barnes, Histone deacetylase-2 and airway disease. *Ther. Adv. Respir. Dis.* **3**, 235–243 (2009).
23. C. Lee, Collaborative power of Nrf2 and PPAR γ activators against metabolic and drug-induced oxidative injury. *Oxid. Med. Cell Longev.* **2017**, 1378175 (2017).
24. S. Polvani, M. Tarocchi, A. Galli, PPAR and oxidative stress: Con(β) catenating NRF2 and FOXO. *PPAR Res.* **2012**, 641087 (2012).
25. R. Brust, H. Lin, J. Fuhrmann, A. Asteian, T. M. Kamenecka, D. J. Kojetin, Modification of the orthosteric PPARγ covalent antagonist scaffold yields an improved dual-site allosteric inhibitor. *ACS Chem. Biol.* **12**, 969–978 (2017).
26. C. L. Sokol, R. B. Camire, M. C. Jones, A. D. Luster, The chemokine receptor CCR8 promotes the migration of dendritic cells into the lymph node parenchyma to initiate the allergic immune response. *Immunity* **49**, 449–463 (2018).
27. D. Martino, S. Prescott, Epigenetics and prenatal influences on asthma and allergic airways disease. *Chest* **139**, 640–647 (2011).
28. W. J. Magner, A. L. Kazim, C. Stewart, M. A. Romano, G. Catalano, C. Grande, N. Keiser, F. Santaniello, T. B. Tomasi, Activation of MHC class I, II, and CD40 gene expression by histone deacetylase inhibitors. *J. Immunol.* **165**, 7017–7024 (2000).
29. Z. Liu, Y. Ren, S. Weng, H. Xu, L. Li, X. Han, A new trend in cancer treatment: The combination of epigenetics and immunotherapy. *Front. Immunol.* **13**, 809761 (2022).
30. J. D. Licht, R. L. Bennett, Leveraging epigenetics to enhance the efficacy of immunotherapy. *Clin. Epigenetics* **13**, 115 (2021).
31. P. Wawrzyniak, M. Wawrzyniak, K. Wanke, M. Sokolowska, K. Bendelja, B. Rückert, A. Globinska, B. Jakiela, J. I. Kast, M. Idzko, M. Akdis, M. Sanak, C. A. Akdis, Regulation of bronchial epithelial barrier integrity by type 2 cytokines and histone deacetylases in asthmatic patients. *J. Allergy Clin. Immunol.* **139**, 93–103 (2017).
32. L. E. P. M. van der Vlugt, K. Eger, C. Müller, D. K. Ninaber, M. C. Zarcone, G. D. Amatngalim, F. Bracher, E. von Mutius, H. H. Smits, P. S. Hiemstra, Farm dust reduces viral load in human bronchial epithelial cells by increasing barrier function and antiviral responses. *J. Allergy Clin. Immunol.* **141**, 1949–1952 (2018).
33. D. Flores-Gomez, W. Hobo, D. van Ens, E. L. Kessler, B. Novakovic, N. Schaap, W. H. C. Rijnen, L. A. B. Joosten, M. G. Netea, N. P. Riksen, S. Bekkering, Interleukin-1β induces trained innate immunity in human hematopoietic progenitor cells in vitro. *Stem Cell Rep.* **19**, 1651–1664 (2024).
34. S. L. Foster, D. C. Hargreaves, R. Medzhitov, Gene-specific control of inflammation by TLR-induced chromatin modifications. *Nature* **447**, 972–978 (2007).
35. P. J. Barnes, Role of HDAC2 in the pathophysiology of COPD. *Annu. Rev. Physiol.* **71**, 451–464 (2009).
36. J. Footitt, P. Mallia, A. L. Durham, W. Eugene Ho, M. B. Trujillo-Torralbo, A. G. Telcian, A. Del Rosario, C. Chang, H. Y. Peh, T. Kebadze, J. Aniscenko, L. Stanciu, S. Essilfie-Quaye, K. Ito, P. J. Barnes, S. L. Elkin, O. M. Kon, W. S. Fred Wong, I. M. Adcock, S. L. Johnston, Oxidative and nitrosative stress and histone deacetylase-2 activity in exacerbations of COPD. *Chest* **149**, 62–73 (2016).
37. W. Liao, A. Y. H. Lim, W. S. D. Tan, J. Abisheganaden, W. S. F. Wong, Restoration of HDAC2 and Nrf2 by andrographolide overcomes corticosteroid resistance in chronic obstructive pulmonary disease. *Br. J. Pharmacol.* **177**, 3662–3673 (2020).
38. A. Croasdell, P. F. Duffney, N. Kim, S. H. Lacy, P. J. Sime, R. P. Phipps, PPAR γ and the innate immune system mediate the resolution of inflammation. *PPAR Res.* **2015**, 549691 (2015).
39. M. Ricote, A. C. Li, T. M. Willson, C. J. Kelly, C. K. Glass, The peroxisome proliferator-activated receptor-γ is a negative regulator of macrophage activation. *Nature* **391**, 79–82 (1998).
40. E. L. Gautier, A. Chow, R. Spanbroek, G. Marcelin, M. Greter, C. Jakubzick, M. Bogunovic, M. Leboeuf, N. van Rooijen, A. J. Habenicht, M. Merad, G. J. Randolph, Systemic analysis of PPARγ in mouse macrophage populations reveals marked diversity in expression with critical roles in resolution of inflammation and airway immunity. *J. Immunol.* **189**, 2614–2624 (2012).
41. M. Marques dos Santos, V. Pivniouk, B. Rankl, A. Walker, G. Pagani, N. Hertkorn, P. Schmitt-Kopplin, C. Müller, F. Bracher, J. Merl-Pham, S. M. Hauck, M. Schloter, A. N. Michael, D. Anderson, L. Honeker, J. Gozdz, O. Pivniouk, C. Ober, M. Holbreich, F. D. Martinez, S. A. Snyder, E. von Mutius, D. Vercelli, Asthma-protective agents in dust from traditional farm environments. *J. Allergy Clin. Immunol.* **152**, 610–621 (2023).
42. M. T. Nakamura, B. E. Yudell, J. J. Loor, Regulation of energy metabolism by long-chain fatty acids. *Prog. Lipid Res.* **53**, 124–144 (2014).
43. B. R. Kwak, S. Myit, F. Mulhaupt, N. Veillard, N. Rufer, E. Roosnek, F. Mach, PPARγ but not PPARα ligands are potent repressors of major histocompatibility complex class II induction in atheroma-associated cells. *Circ. Res.* **90**, 356–362 (2002).
44. G. Pascual, A. L. Fong, S. Ogawa, A. Gamliel, A. C. Li, V. Perissi, D. W. Rose, T. M. Willson, M. G. Rosenfeld, C. K. Glass, A SUMOylation-dependent pathway mediates transrepression of inflammatory response genes by PPAR-γ. *Nature* **437**, 759–763 (2005).
45. S. Ghisletti, W. Huang, S. Ogawa, G. Pascual, M. E. Lin, T. M. Willson, M. G. Rosenfeld, C. K. Glass, Parallel SUMOylation-dependent pathways mediate gene- and signal-specific transrepression by LXRs and PPARγ. *Mol. Cell* **25**, 57–70 (2007).
46. A. Mottis, L. Mouchiroud, J. Auwerx, Emerging roles of the corepressors NCoR1 and SMRT in homeostasis. *Genes Dev.* **27**, 819–835 (2013).
47. G. John-Schuster, K. Hager, T. M. Conlon, M. Irmler, J. Beckers, O. Eickelberg, A. Ö. Yildirim, Cigarette smoke-induced iBALT mediates macrophage activation in a B cell-dependent manner in COPD. *Am. J. Physiol. Lung Cell Mol. Physiol.* **307**, L692–L706 (2014).
48. S. Orchard, M. Ammari, B. Aranda, L. Breuza, L. Briganti, F. Broackes-Carter, N. H. Campbell, G. Chavali, C. Chen, N. Del-Toro, M. Duesbury, M. Dumousseau, E. Galeota, U. Hinz, M. Iannuccelli, S. Jagannathan, R. Jimenez, J. Khadake, A. Lagreid, L. Licata, R. C. Lovering, B. Meldal, A. N. Melidoni, M. Milagros, D. Peluso, L. Perfetto, P. Porras, A. Raghunath, S. Ricard-Blum, B. Roechert, A. Stutz, M. Tognolli, K. Van Roey, G. Cesareni, H. Hermjakob, The MIntAct project—IntAct as a common curation platform for 11 molecular interaction databases. *Nucleic Acids Res.* **42**, D358–D363 (2014).
49. M. E. Cusick, H. Yu, A. Smolyar, K. Venkatesan, A. R. Carvunis, N. Simonis, J. F. Rual, H. Borick, P. Braun, M. Dreze, J. Vandenhaute, M. Galli, J. Yazaki, D. E. Hill, J. R. Ecker, F. P. Roth, M. Vidal, Literature-curated protein interaction datasets. *Nat. Methods* **6**, 39–46 (2009).
50. A. J. M. Walhout, R. Sordella, X. Lu, J. L. Hartley, G. F. Temple, M. A. Brasch, N. Thierry-Mieg, M. Vidal, Protein interaction mapping in *C. elegans* using proteins involved in vulval development. *Science* **287**, 116–122 (2000).
51. K. Luck, D. K. Kim, L. Lambourne, K. Spirohn, B. E. Begg, W. Bian, R. Brignall, T. Cafarelli, F. J. Campos-Laborie, B. Charloteaux, D. Choi, A. G. Coté, M. Daley, S. Deimling, A. Desbuleux, A. Dricot, M. Gebbia, M. F. Hardy, N. Kishore, J. J. Knapp, I. A. Kovács, I. Lemmens, M. W. Mee, J. C. Mellor, C. Pollis, C. Pons, A. D. Richardson, S. Schlabach, B. Teeking, A. Yadav, M. Babor, D. Balcha, O. Basha, C. Bowman-Colin, S. F. Chin, S. G. Choi, C. Colabella, G. Coppin, C. D'Amata, D. De Ridder, S. De Rouck, M. Duran-Frigola, H. Ennajdaoui, F. Goebels, L. Goehring, A. Gopal, G. Haddad, E. Hatchi, M. Helmy, Y. Jacob, Y. Kassa, S. Landini, R. Li, N. van Lieshout, A. MacWilliams, D. Markey, J. N. Paulson, S. Rangarajan, J. Rasla, A. Rayhan, T. Rolland, A. San-Miguel, Y. Shen, D. Sheykhkarimli, G. M. Sheynkman, E. Simonovsky, M. Taşan, A. Tejeda, V. Tropepe, J. C. Twizere, Y. Wang, R. J. Weatheritt, J. Weile, Y. Xia, X. Yang, E. Yeger-Lotem, Q. Zhong, P. Aloy, G. D. Bader, J. D. L. Rivas, S. Gaudet, T. Hao, J. Rak, J. Tavernier, D. E. Hill, M. Vidal, F. P. Roth, M. A. Calderwood, A reference map of the human binary protein interactome. *Nature* **580**, 402–408 (2020).
52. E. L. Huttlin, R. J. Bruckner, J. Navarrete-Perea, J. R. Cannon, K. Baltier, F. Gebreab, M. P. Gygi, A. Thornock, G. Zarraga, S. Tam, J. Szpyt, B. M. Gassaway, A. Panov, H. Parzen, S. Fu, A. Golbazi, E. Maenpaa, K. Stricker, S. Guha Thakurta, T. Zhang, R. Rad, J. Pan, D. P. Nusinow, J. A. Paulo, D. K. Schweppe, L. P. Vaites, J. W. Harper, S. P. Gygi, Dual proteome-scale networks reveal cell-specific remodeling of the human interactome. *Cell* **184**, 3022–3040 (2021).
53. J. D. Zhang, S. Wiemann, KEGGgraph: A graph approach to KEGG PATHWAY in R and bioconductor. *Bioinformatics* **25**, 1470–1471 (2009).
54. M. Milacic, D. Beavers, P. Conley, C. Gong, M. Gillespie, J. Griss, R. Haw, B. Jassal, L. Matthews, B. May, R. Petryszak, E. Ragueneau, K. Rothfels, C. Sevilla, V. Shamovsky, R. Stephan, K. Tiwari, T. Varusai, J. Weiser, A. Wright, G. Wu, L. Stein, H. Hermjakob, P. D'Eustachio, The reactome pathway knowledgebase 2024. *Nucleic Acids Res.* **52**, D672–D678 (2024).
55. A. T. Kalinka, P. Tomancak, linkcomm: An R package for the generation, visualization, and analysis of link communities in networks of arbitrary size and type. *Bioinformatics* **27**, 2011–2012 (2011).
56. Y. Y. Ahn, J. P. Bagrow, S. Lehmann, Link communities reveal multiscale complexity in networks. *Nature* **466**, 761–764 (2010).
57. K. Héberger, K. Kollár-Hunek, Sum of ranking differences for method discrimination and its validation: Comparison of ranks with random numbers. *J. Chemom.* **25**, 151–158 (2011).

58. Y. Zhang, T. Liu, C. A. Meyer, J. Eeckhoute, D. S. Johnson, B. E. Bernstein, C. Nussbaum, R. M. Myers, M. Brown, W. Li, X. S. Shirley, Model-based analysis of ChIP-Seq (MACS). *Genome Biol.* **9**, R137 (2008).
59. E. Z. Macosko, A. Basu, R. Satija, J. Nemesh, K. Shekhar, M. Goldman, I. Tirosh, A. R. Bialas, N. Kamitaki, E. M. Martersteck, J. J. Trombetta, D. A. Weitz, J. R. Sanes, A. K. Shalek, A. Regev, S. A. McCarroll, Highly parallel genome-wide expression profiling of individual cells using nanoliter droplets. *Cell* **161**, 1202–1214 (2015).
60. M. D. Luecken, F. J. Theis, Current best practices in single-cell RNA-seq analysis: A tutorial. *Mol. Syst. Biol.* **15**, e8746 (2019).

Acknowledgments: We would like to thank C. Hollauer, A. Housni, S. Havristiuc, K. Caglar, N. Patil, C. Goracci, L. Theilacker, and E. Primerano for technical assistance and helpful discussions. **Funding:** This study was supported by the German Center for Lung Research (DZL) (A.Ö.Y. and E.v.M.), ERC Advanced Grant (APROSUS–101052876) (E.v.M.), ERC Starting Grant (ERC-2016-STG-715182) (B.U.S.), TRR 359/B05–project number 491676693 (B.U.S.), European Union's Horizon 2020 Research (P.F.-B.), and Innovation Programme (Project ID 101137201) (P.F.-B.).
Author contributions: Conceptualization: A.Ö.Y. and E.v.M. Methodology: A.Ö.Y., E.v.M., G.D., M.K., and S.C. Data acquisition and analysis: G.D., M.K., S.C., Z.E., X.T., S.S., U.R.K., S.S., B.R., A.J., D.D., L.L., and M.W. scRNA-seq preprocessing and annotation: Y.C., C.H.M., A.A., and T.S.K. Downstream bioinformatics analysis: G.D., D.D., J.O., and T.S.K. Mouse PPI Network construction and analysis: C.-W.L. and P.F.-B. Key intellectual input and experimental tools: H.S., P.F.-B., T.M.C., A.J., and H.W. Writing—original draft: G.D., A.Ö.Y., T.M.C., and A.J. Writing—review: A.J., S.C., A.Ö.Y., T.M.C., and E.v.M. All authors edited the manuscript. All authors read and approved the final manuscript. **Competing interests:** E.v.M. has patent no. PCT/EP2019/085016 pending, royalties paid to ProtectImmun for patent EP2361632 (granted on 19 March 2014) and patents EP1411977 (granted on 18 April 2007), EP1637147 (granted on 10 December 2008), and EP 1964570 (granted on 21 November 2012) licensed to ProtectImmun. E.v.M., A.Ö.Y., H.A., B.R., and C.M. are included in the following patents: patent EP21189353.2. 2021 and patent PCT/US2021/016918. E.v.M. received grants or contracts from the following: Bavarian State Ministry of Health and Care for "URS Study"; "Impact Chip Study," OM Pharma S.A.; Go Bio Initial Grant, BMBF (Federal Ministry of Education and Research); European Research Council Award; and "BEAR Study," O.M. Pharma S.A. E.v.M. received royalties or licenses from the following: Elsevier GmbH, Georg Thieme Verlag, Springer-Verlag GmbH, Elsevier Ltd., Springer Nature Group, and Deutscher Apotheker Verlag. E.v.M. received consulting fees from the following: Chinese University of Hongkong, European Commission, AstraZeneca, Imperial College London, and OM Pharma S.A. E.v.M. has received payment or honoraria for lectures, presentations, speakers bureaus, manuscript writing, or educational events from the following: ALK-Abello Arzneimittel GmbH, Japanese Society of Pediatric Allergy and Clinical Immunology (JSPACI), Klinikum Rechts der Isar, University of Colorado, Paul-Martini-Stiftung, Astra Zeneca BioPharmaceuticals Medical, Imperial College London, Children's Hospital Research Institute of Manitoba Kompetenzzentrum für Ernährung (Kern), OM Pharma S.A., Swedish Pediatric Society for Allergy and Lung Medicine, Chinese College of Allergy and Asthma (CCAA), Abbott Laboratories, Deutscher Apotheker Verlag GmbH & Co. KG, Socieded Chilena de Enfermedades Respiratorias, Japanese Society of Allergology, British Society for Asthma and Clinical Immunology, American Academy of Allergy, Asthma & Immunology, European Respiratory Society (ERS), and Ludwig Maximilians University Munich. The authors declare that they have no other competing interests. **Data, code, and materials availability:** All data and code needed to evaluate and reproduce the results in the paper are present in the paper and/or the Supplementary Materials. Generated data are publicly available online under the acession numbers mentioned here: scRNA-seq and ATAC-seq data were submitted to the NCBI Gene Expression Omnibus (GEO) database (www.ncbi.nlm.nih.gov/geo/). scRNA-seq data have the accession number (GSE307573), and ATAC-seq data have the number (GSE308681). Bulk RNA-seq data for this study have been deposited in the European Nucleotide Archive (ENA) at EMBL-EBI under accession number PRJEB102197 (www.ebi.ac.uk/ena/browser/view/PRJEB102197). This study did not generate new materials.

Submitted 3 May 2025
Accepted 22 January 2026
Published 27 February 2026
10.1126/sciadv.ady7317

ScienceAdvances

A beneficial environment promotes immune resilience through epigenetic regulation

Guilherme Dragunas, Markus Klotz, Sirui Chen, Zeynep Ertüz, Xiaomei Tan, Ülkü Rabia Korkmaz, Soni Shankhwar, Bettina Rankl, Deepesh Dhakad, Jimmy Omony, Christoph H. Mayr, Yuexin Chen, Ahmed Agami, Chung-Wen Lin, Christoph Müller, Lars Lunding, Michael Wegmann, Johanna Berner, Jelena Popovic, Barbara U. Schraml, Heiko Adler, Pascal Falter-Braun, Herbert Schiller, Henrik Watz, Thomas M. Conlon, Aicha Jeridi, Theodoros S. Kapellos, Erika von Mutius, and Ali Önder Yildirim

Sci. Adv. **12** (9), eady7317. DOI: 10.1126/sciadv.ady7317

Science Advances (ISSN 2375-2548) is published by the American Association for the Advancement of Science. 1200 New York Avenue NW, Washington, DC 20005. The title *Science Advances* is a registered trademark of AAAS.